

## Supplementary Materials for controlled non-radical chlorine activation pathway on hematite photoanodes for efficient oxidative chlorination reactions

Daojian Tang,<sup>a,c†</sup> Lei Wu,<sup>a,c†</sup> Liubo Li,<sup>b</sup> Niankai Fu,<sup>b,c</sup> Chuncheng Chen,<sup>a,c</sup> Yuchao Zhang<sup>\*a,c</sup> and Jincai Zhao<sup>a,c</sup>

<sup>a</sup> Key Laboratory of Photochemistry, Beijing National Laboratory for Molecular Sciences, Institute of Chemistry, Chinese Academy of Sciences, Beijing 100190, P. R. China.

<sup>b</sup> Key Laboratory of Molecular Recognition and Function, Beijing National Laboratory for Molecular Sciences, Institute of Chemistry, Chinese Academy of Sciences, Beijing 100190, P. R. China.

<sup>c</sup> University of Chinese Academy of Sciences, Beijing 100049, P. R. China.

\* Corresponding author. Email: [yczhang@iccas.ac.cn](mailto:yczhang@iccas.ac.cn)

† [These authors contributed equally.](#)

## Experimental Details

**Materials:** Fluorine-doped tin oxide substrates (FTO, 2.2 mm) were purchased from Nippon Plate Glass Co., Ltd. Iron (III) chloride anhydrous (98%) and titanium (IV) butoxide (97%) was purchased from Alfa Aesar. Sodium perchlorate (99%) and sodium nitrate (99%) were purchased from Acros Organics. Titanium tetrachloride (99.9%), sodium chloride (99.9%), acetanilide (99%), tetraethylammonium tetrafluoroborate (NEtBF<sub>4</sub>, 98%) and acetonitrile (99.9 %, extra dry with molecular sieves, Water≤50 ppm) were purchased from Innochem. All chemicals were used as received without further purification.

**Instrumentation:** X-ray diffraction (XRD) patterns was collected on an X-ray diffractometer (Empyrean, PANalytical) with Cu - K $\alpha$  radiation at a scan rate of 0.05° 2 $\theta$  s<sup>-1</sup>. Scanning electron microscopy (SEM) images were obtained with an SU8010 (Hitachi, Japan). X-ray photoelectron spectroscopy (XPS) data was collected on an ESCALAB 250Xi spectrometer equipped with 300 W Al K $\alpha$  radiation. Adventitious carbon with the binding energy of 284.8 eV was used as a reference for calibration. UV-vis spectra were recorded with a UV-vis Hitachi U-3900 spectrophotometer. X-ray absorption fine structure spectra (XAFS) were obtained at the Beijing Synchrotron Radiation Facility (1W1B). The energy was calibrated by a standard Fe foil before each experiment. The high-resolution transmission electron microscopy (HRTEM) images and elemental mappings were recorded with a high-resolution transmission electron microscope (Thermo Fisher Scientific, FEI Talos 200X) operated at 200 kV. High-performance liquid chromatography (HPLC) was conducted using Agilent 1260

infinities system. Chromatography-mass spectrometry (GC-MS) was conducted using an Agilent GC-MS instrument (5977A MSD and 7890B GC system). Nuclear magnetic resonance (NMR) spectra were measured on a Bruker 400 MHz instrument. Photoelectrochemical (PEC) measurements were controlled by a CHI 1040c potentiostat. The electrochemical impedance spectroscopy (EIS) and intensity modulated photocurrent spectroscopy (IMPS) experiments were performed with a potentiostat (PGSTAT302N autolab, Metrohm).

**Photoanodes preparation:** Hematite( $\alpha$ - $\text{Fe}_2\text{O}_3$ ) photoanodes were fabricated in accordance with our previously reported procedures.<sup>1</sup> FTO substrates were first cleaned with acetone, ethanol and deionized water by ultrasonication for 30 min. 7.5 mL aqueous solution containing 0.15 M  $\text{FeCl}_3$ , 0.1 M  $\text{NaNO}_3$  and 9  $\mu\text{L}$  of 0.5 M  $\text{TiCl}_4$  solution were prepared in a Teflon-lined stainless-steel autoclave. Cleaned FTO substrates were placed in the autoclave and heated at 95°C for 4 h. After the hydrothermal treatment, a uniform layer of Ti-doped iron oxyhydroxides (Ti:FeOOH) was coated on the FTO glass, which was washed with deionized water to remove any residual salts. The obtained films were annealed in air at 550°C for 2 h and annealed at 650°C for 20 min to convert the Ti:FeOOH nanowires into Ti-doped  $\alpha$ - $\text{Fe}_2\text{O}_3$  nanowires. Subsequently, the second growth of Ti:FeOOH layer on the obtained Ti-doped  $\alpha$ - $\text{Fe}_2\text{O}_3$  nanowires was performed in the same conditions but with half the precursors and adding 375  $\mu\text{L}$  of 0.15 M  $\text{NH}_4\text{F}$ . Finally, the as-prepared Ti: $\alpha$ - $\text{Fe}_2\text{O}_3$ @Ti:FeOOH nanowires were further annealed at 550°C for 2 h and annealed at 650 °C for 20 min to prepare Ti-doped  $\alpha$ - $\text{Fe}_2\text{O}_3$  nanowires.

TiO<sub>2</sub> photoanodes were synthesized using a previously reported method.<sup>2</sup> 15 mL of deionized water and 15 mL of concentrated HCl (37 wt %) were mixed in a 100 mL beaker followed by addition of 500 μL of Ti(IV) butoxide and stirred for 30 min. Then, 7.5 ml of mixed precursor solution was transferred into a Teflon-lined stainless-steel autoclave. Cleaned FTO substrates were placed in the autoclave and heated in an oven at 150°C for 6 h. The obtained films were annealed in air at 450°C for 1.5 h to improve the crystallinity of TiO<sub>2</sub> nanorods and enhance their contact to the FTO substrate.

**PEC measurement:** PEC experiments were performed in a three-electrode electrochemical cell with Pt as the counter electrode and Ag/AgCl as the reference electrode. Nafion proton exchange membrane was used to separate the photoanode from the cathode chamber. Under general reaction conditions, PEC electrolysis measurements were conducted in a 10 mL solution of CH<sub>3</sub>CN/H<sub>2</sub>O (1:1, v/v) containing 0.1 M NaCl (pH 6.4), 0.1 mmol of substrate under AM1.5 G simulated sunlight obtained by a Xenon lamp with an AM 1.5 G filter. Photoelectrolysis was performed with magnetic stirring at 900 rpm, and a water recycling system was used to prevent the solution from heating up during photoelectrolysis. For EIS measurements, a 470 nm LED lamp was used as the light source for α-Fe<sub>2</sub>O<sub>3</sub>, and a 365nm LED lamp was used for TiO<sub>2</sub>. The measurements were conducted over a frequency range from 10<sup>4</sup> Hz to 0.1 Hz. For IMPS measurements, a light intensity of 100 mW cm<sup>-2</sup> with a 10% modulation intensity was used, and the frequency was varied from 10<sup>4</sup> Hz to 0.1 Hz with 20 points per decade. EIS and IMPS experimental data were fitted and simulated using Nova 2.1.4 from Metrohm Inc. Unless otherwise specified, the tests were conducted without

iR compensation and in a non-conditioned air atmosphere.

**Oxygen (O<sub>2</sub>) detection:** The PEC electrolysis experiments with different Cl<sup>-</sup> concentration were conducted after purged with Ar (15 sccm) for 15 min in a sealed H-type cell. After 1 h electrolysis, 1.0 mL of gas products from PEC electrolysis on the headspace (9.6 mL) of anode chamber were analyzed using a gas chromatograph (GC, 9790plus, Ar carrier, Fuli) equipped with a thermal conductivity detector (TCD). The volume of the headspace in the anode chamber was calculated by a drainage water method. The non-absolute tightness allows air to inevitably enter the cell. The extra oxygen from the air was subtracted based on the quantity of nitrogen (N<sub>2</sub>) content in the anode chamber, with a ratio of 1:3.7. To obtain the calibration curve of O<sub>2</sub> and N<sub>2</sub>, different volumes (0~1 mL) of O<sub>2</sub> and N<sub>2</sub> standard gas were quantified by GC. According to the ideal gas law, the moles of O<sub>2</sub> and N<sub>2</sub> standard gas can be calculated, and the calibration curve of O<sub>2</sub> and N<sub>2</sub> (i.e., peak area against moles of O<sub>2</sub> standard gas) was thus obtained (**Fig. S5**). The Faradaic efficiency of O<sub>2</sub>,  $FE(O_2)$ , could be calculated by the following equation:

$$FE(O_2) = \frac{\left[ n_{O_2}(mol) - \frac{n_{N_2}(mol)}{3.7} \right] \times 4 \times F(96500 C/mol)}{Q(C)} \times 100\%$$

where 3.7 was the ratio of N<sub>2</sub> to O<sub>2</sub> in the air. 4 was the number of transferred electrons for O<sub>2</sub>. F was the Faradaic constant and equal to 96500 C mol<sup>-1</sup>, and Q represented the passed charge during the photoelectrolysis.

**Active chlorine detection:** The concentration of produced active chlorine was

quantitated by using the N, N-diethyl-p-phenylenediamine (DPD) method.<sup>3</sup> Specifically, DPD reagent solution (250 mM, 50 mL) was prepared by the addition of 3.28 g DPD in 0.05 M H<sub>2</sub>SO<sub>4</sub>, and stored in dark. After the electrolysis reaction, take 1.0 mL of electrolyte and dilute it with deionized water to a total volume of 10 mL. Then, add 1 mL of phosphoric acid buffer (pH = 6.5) and 1.0 mL of DPD reagent to the solution. Subsequently, measure the fully mixed solution using a UV-vis spectrometer as soon as possible at an absorbance wavelength of 550 nm. The calibration curve was plotted from absorbance versus the concentration of ClO<sup>-</sup> (**Fig. S6a**). The active chlorine selectivity was calculated according to the following equation:

$$\text{FE} = \frac{2nF}{Q} \times 100\%$$

where 2 was the number of transferred electrons for active Cl<sup>+</sup> species, n was the amount of detected active Cl<sup>+</sup> species by DPD method, F was the Faradaic constant (96500 C mol<sup>-1</sup>), Q was the passed charge.

**Electron paramagnetic resonance (EPR) measurements:** 5,5-dimethyl-1-pyrroline N-oxide (DMPO) was used as the spin-trap reagent to capture the possible radicals that generated in the photoelectrolysis. To *in-situ* trap those radicals, an open-type cell (**Fig. S34**) was used based on the previously reported method.<sup>1</sup> In general, 10 μL DMPO solution was added onto the photoanode surface through a pipette during the photoelectrolysis. Notably, the pipette and photoanodes needed to be in close contact. If radicals were produced during photoelectrolysis, they would react with DMPO *in situ* to form corresponding species. Afterwards, the final solution was promptly collected

for EPR measurements.

**Substrate generation/tip collection mode of scanning electrochemical microscope**

**(SG/TC SECM) measurement for Cl<sub>2</sub> detection:** The measurement method was in accordance with our previously reported procedures.<sup>1</sup> The SG/TC SECM was performed on the Sensolytics SECM instrument consisting of a stepper-motor positioning system (Sensolytics, BsaeseCM), a Xenon lamp source (Ceaulight, CEL-HXF300-T3) and a bipotentiostat (Metrohm, Autolab PGSTAT302N). The Cl<sub>2</sub> detection were performed in a four-electrode cell with a coiled Pt wire as the counter electrode, a saturated Ag/AgCl electrode as the reference electrode, a Pt-disk ultramicroelectrode (UME) with a diameter of 25 μm as working electrode 1 (WE1, also called tip electrode), and α-Fe<sub>2</sub>O<sub>3</sub> or TiO<sub>2</sub> as working electrode 2 (WE2, also called substrate electrode). The status of the probe was checked by the CV measurement in a 0.1 M KCl solution containing 5 mM K[Fe(CN)<sub>6</sub>] as redox mediator. Subsequently, an applied potential of -0.2 V vs. Ag/AgCl was applied to the tip electrode for the approach curve measurement. By fitting the negative feedback approach curve to the theoretical equations,<sup>4, 5</sup> the distance scale between tip electrode and substrate electrode was approximately 13 μm for both α-Fe<sub>2</sub>O<sub>3</sub> and TiO<sub>2</sub> as substrate electrode. Finally, a potential sweep (5 mV s<sup>-1</sup>) from -0.2 to 1.2 V vs. Ag/AgCl was conducted on the substrate electrode, while maintaining a constant potential of 0.3 V vs. Ag/AgCl for the tip electrode to monitor the Cl<sub>2</sub> reduction current.

**Product analysis:** All the products generated by PEC reactions were analyzed by GC-MS or NMR to confirm the identity. The GC-MS measurements were run on an Agilent

GC-MS instrument with a HP-5ms GC column and electron ionization ion source. The solvent delay time was 3 min. For acetanilide (**1a**), the chlorination products were quantified by HPLC. Measurements were run on an Agilent HPLC instrument with a C18 column and DAD detector. Detection wavelength was 240 nm and mobile phase ratio was 70% H<sub>2</sub>O: 30% CH<sub>3</sub>CN. The chlorination products (**2-6**) were quantified by GC. Measurements were run on an Agilent GC instrument with a DB-VRX GC column and FID detector. The chlorination products (**7-11**, **13-15**) were quantified by NMR analysis with 1,3,5-trimethoxybenzene as the internal standard substrate after extraction treatment by ethyl acetate.

The values of selectivity, faradaic efficiency and conversion rate were calculated by the following equations:

$$\text{Selectivity} = \frac{\text{content of corresponding product}}{\text{consumption of reactant}} \times 100\%;$$

Faradaic efficiency (FE) =  $\frac{2nF}{Q} \times 100\%$  (where n was the productivity of products, F was the Faradaic constant), and Q was the quantity of electric charge);

Yield rate =  $\frac{\text{the productivity of products}}{t \times A}$  (where t is the reaction time, and A is the area of photoanode (2 cm<sup>-2</sup>)).

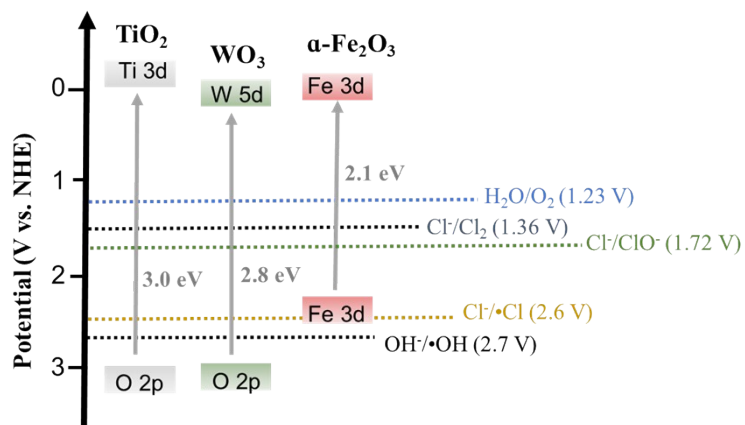


**Fig. S1.** Bandgaps and band edge positions of TiO<sub>2</sub>, WO<sub>3</sub> and α-Fe<sub>2</sub>O<sub>3</sub> with respect to the energy position of redox couples involving O<sub>2</sub>, Cl<sub>2</sub>, ClO<sup>-</sup>, •Cl, and •OH.<sup>6-8</sup>

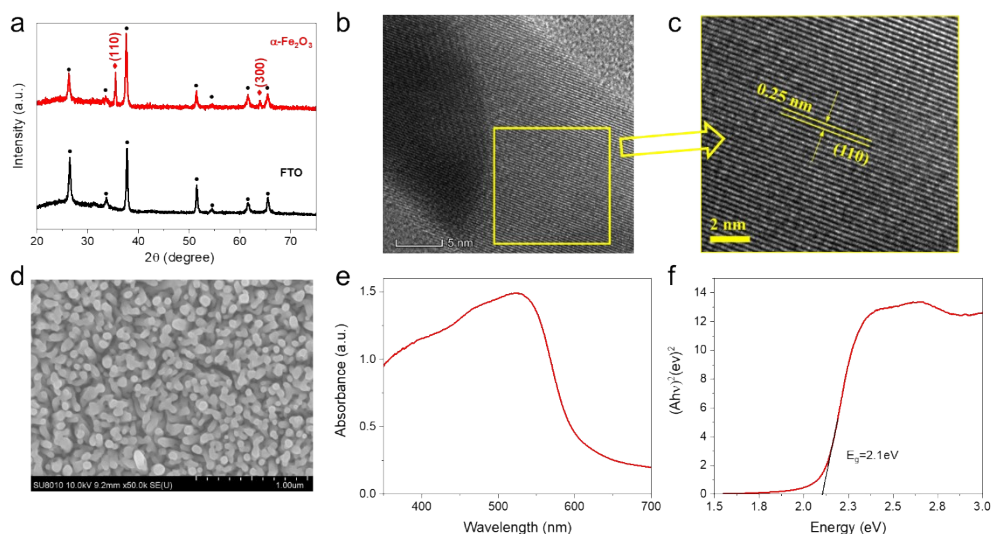


**Fig. S2.** Structural characterizations of  $\alpha$ -Fe<sub>2</sub>O<sub>3</sub>. (a) XRD patterns, (b-c) HRTEM images and (d) SEM image of an  $\alpha$ -Fe<sub>2</sub>O<sub>3</sub> photoanode. (e) UV-vis spectrum and (f) the corresponding Tauc plot of an  $\alpha$ -Fe<sub>2</sub>O<sub>3</sub> photoanode.

According to the previous reports, the diffraction peaks at  $2\theta = 35.6^\circ$  and  $64.0^\circ$  were indexed to the (110) and (300) planes of the  $\alpha$ -Fe<sub>2</sub>O<sub>3</sub> phase.<sup>1, 9-11</sup> No other reflection was observed, indicating the oriented growth of  $\alpha$ -Fe<sub>2</sub>O<sub>3</sub> nanorods with respect to the FTO substrate. Furthermore, the lattice fringes of 0.25 nm attributed to the (110) plane of  $\alpha$ -Fe<sub>2</sub>O<sub>3</sub> could be well resolved in the HRTEM image.<sup>12, 13</sup> The SEM image of  $\alpha$ -Fe<sub>2</sub>O<sub>3</sub> photoanodes indicated that the as-prepared  $\alpha$ -Fe<sub>2</sub>O<sub>3</sub> film consisted of numerous nanorods. Subsequent UV-vis spectrum highlighted the excellent visible light absorption of the as-prepared sample. And the corresponding Tauc plot gave a narrow optical band gap of 2.1 eV, consistent with the reported values in the literature.<sup>14-16</sup> These results confirmed the successful fabrication of  $\alpha$ -Fe<sub>2</sub>O<sub>3</sub> photoanodes.

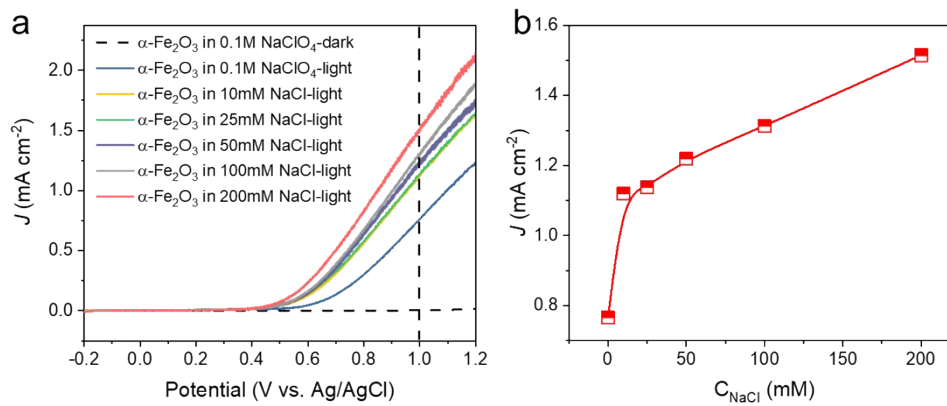


**Fig. S3.** The effect of  $\text{Cl}^-$  concentrations on the photocurrent. (a) LSV curves (50 mV/s) at varying  $\text{Cl}^-$  concentrations. (b) The photocurrent behavior was observed at 1.0 V vs. Ag/AgCl with different concentration of  $\text{Cl}^-$ . The total concentration of  $\text{Na}^+$  was kept at 0.1 M by adding  $\text{NaClO}_4$  when the  $\text{Cl}^-$  concentration was below 0.1 M.

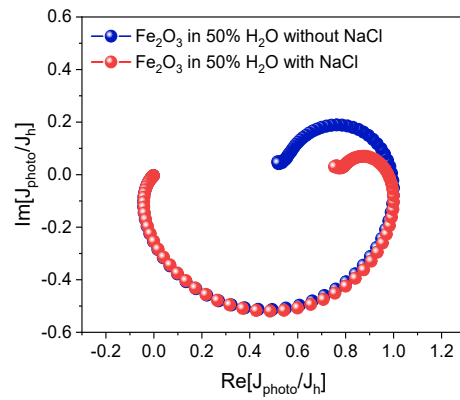


**Fig. S4.** IMPS measurements. The normalized IMPS spectra of an  $\alpha$ - $\text{Fe}_2\text{O}_3$  photoanode at 1.0 V vs. Ag/AgCl in 0.1 M  $\text{NaClO}_4$  without or with 10 mM NaCl under 470 nm irradiation.

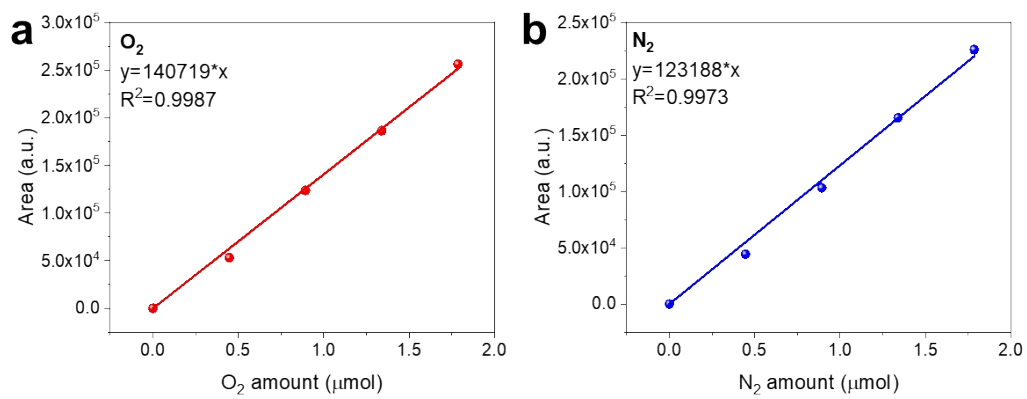


**Fig. S5.** The calibration curves of (a) O<sub>2</sub> and (b) N<sub>2</sub>.

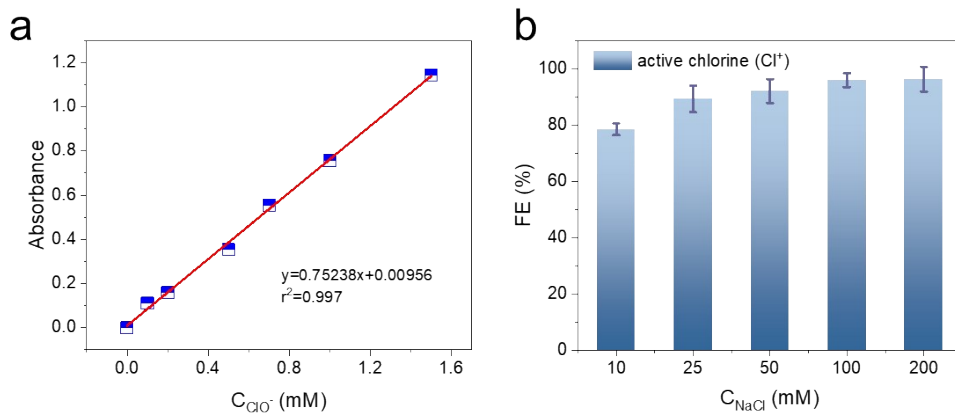


**Fig. S6.** The selectivity of  $\text{Cl}^-$  oxidation on an  $\alpha\text{-Fe}_2\text{O}_3$  photoanode. (a) The standard curve of absorbance against the concentration of  $\text{ClO}^-$ . (b) The FE of  $\text{Cl}^-$  oxidation after 10 min of photoelectrolysis at 1.0 V vs. Ag/AgCl with different concentrations of  $\text{Cl}^-$  in a  $\text{CH}_3\text{CN}/\text{H}_2\text{O}$  (1:1 v/v) solution.

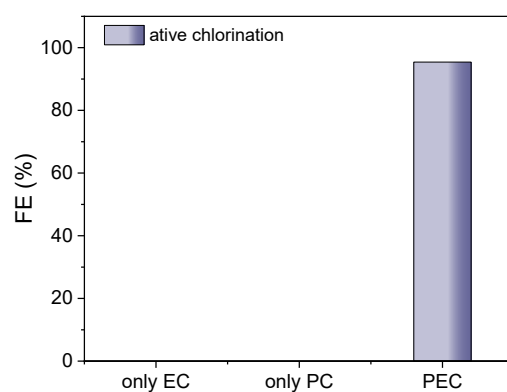


**Fig. S7.** Performance of  $\text{Cl}^-$  oxidation in the EC system only, PC system only, and PEC system. The electrochemical (EC) experiment was carried out in 0.1 M NaCl solution at 1.0 V vs. AgCl for 10 min. The photochemical (PC) experiment was carried out in 0.1 M NaCl solution under AM 1.5G irradiation for 10 min. The PEC experiment was performed in 0.1 M NaCl solution under AM 1.5G irradiation at 1.0 V vs. AgCl for 10 min.

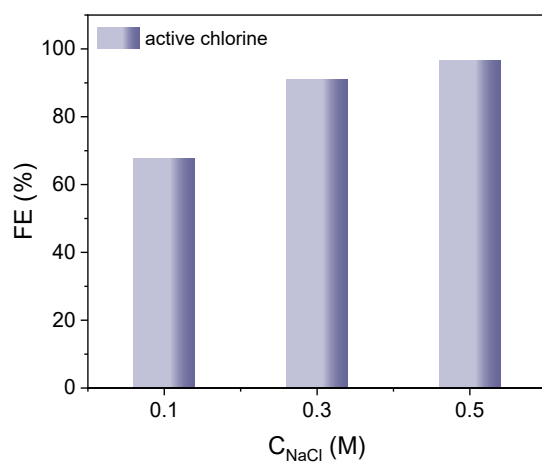


**Fig. S8.** The FE of  $\text{Cl}^-$  oxidation after 10 min of photoelectrolysis at 1.0 V vs. Ag/AgCl with different concentrations of  $\text{Cl}^-$  in an aqueous solution.

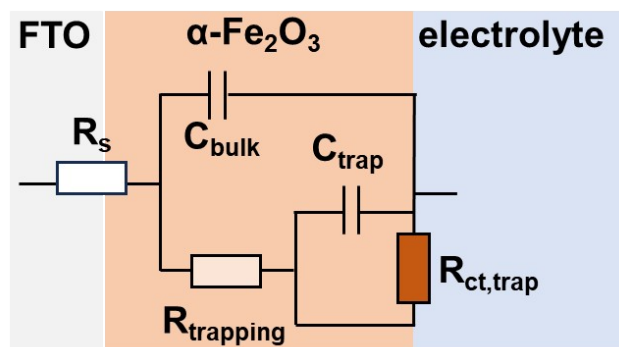


**Fig. S9.** The equivalent model circuit for EIS fit and simulation.

Hamann and co-workers have proven that the surface reaction on the  $\alpha\text{-Fe}_2\text{O}_3$  photoanode mainly takes place from surface trapped holes (i.e., high-valent iron-oxo species), and not directly from valence band holes through the EIS analysis.<sup>17, 18</sup> And they also established an EIS method including the equivalent circuit (**Fig. S9**) to investigate the role of surface states. In this model,  $R_{\text{trapping}}$  represents the resistance in surface hole trapping,  $R_{\text{ct,trap}}$  represents the charge transfer resistance via surface states, and  $C_{\text{trap}}$  represents the hole accumulated at surface states (surface-state capacitance). The Nyquist plots exhibit two semicircles for this model. The high-frequency semicircle represents the process of hole trapping by surface states (hole accumulation at surface states), while the radius of the low-frequency semicircle reflects the process of interfacial hole transfer to electrolyte for substrate oxidation. we also exploited the equivalent circuit displayed in **Fig. S9** to fit EIS data with Nova 2.1.4 software (Metrohm). The fitted data for water oxidation and chlorine oxidation could be found in **Table S3** and **Table S4**, which allows us to obtain the surface-state capacitance shown in **Fig. 1f**.

To understand the effect of surface hole density on the reaction pathway, rate law

analysis was conducted by modulating the illumination intensity during EIS measurements. The water oxidation and  $\text{Cl}^-$  oxidation rate can be estimated from the steady-state photocurrent density ( $J$ ), and the surface-trapped hole density [hole] can be estimated from the following equation:<sup>19, 20</sup>

$$[\text{hole}] = C_{\text{trap}} \times V_{\text{appl}} \times \frac{R_{\text{ct, trap}}}{R_s \times R_{\text{trapping}} \times R_{\text{ct, trap}}} / S$$

where  $V_{\text{appl}}$  is the applied potential and  $S$  is the active area of the  $\alpha\text{-Fe}_2\text{O}_3$  photoanode.

Correspondingly, the reaction order of surface holes can be calculated by the following equation:

$$J = k [\text{hole}]^\beta$$

where  $k$  is the rate constant of the reaction, and  $\beta$  is the reaction order.

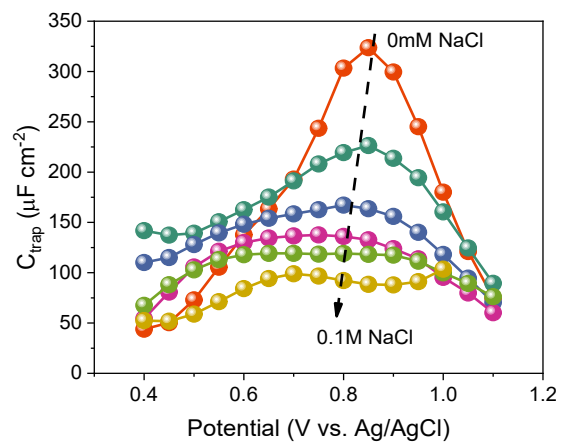


**Fig. S10.** The behavior of  $C_{\text{trap}}$  with different concentrations of  $\text{Cl}^-$ .

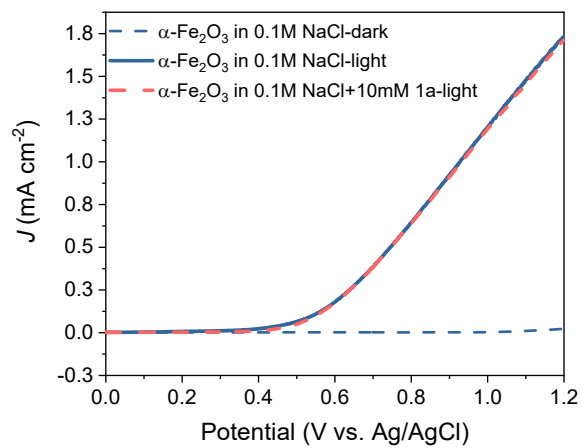


**Fig. S11.** LSV curves of an  $\alpha$ -Fe<sub>2</sub>O<sub>3</sub> photoanode under AM 1.5G irradiation measured in 0.1 M NaCl solution with and without 10 mM **1a**.

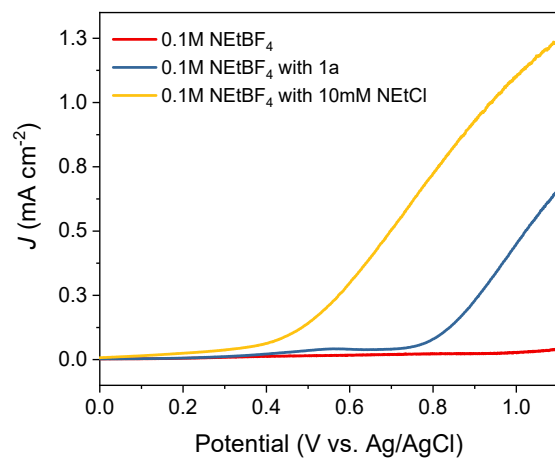


**Fig. S12.** LSV curves of the oxidation of Cl<sup>-</sup> and **1a** in a 100% MeCN solution with 0.1M NEtBF<sub>4</sub> as the supporting electrolyte under AM 1.5G irradiation.

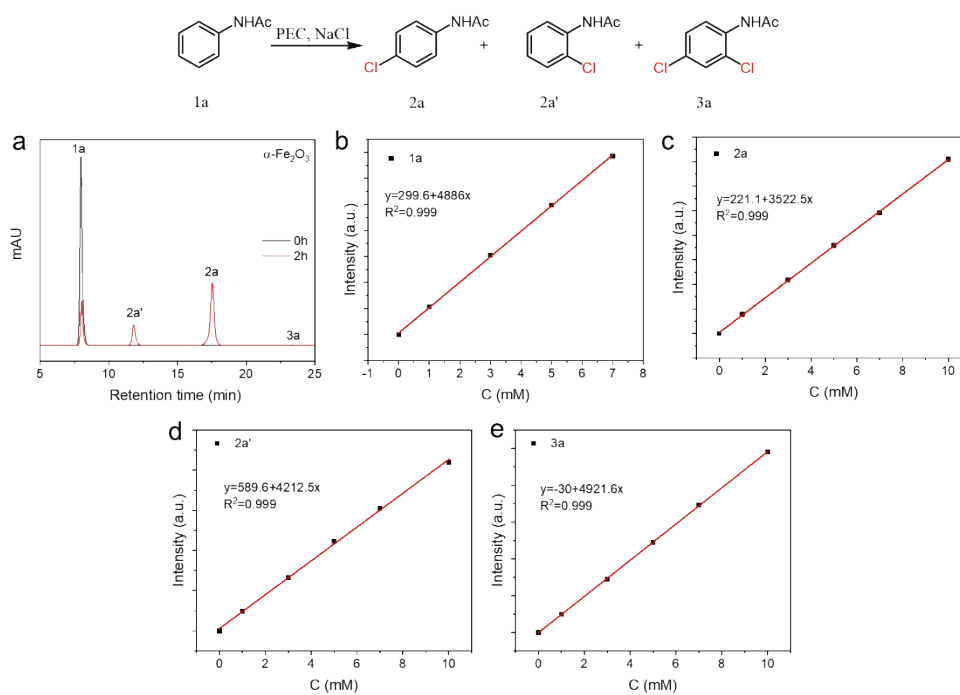


**Fig. S13.** The quantification of aromatic chlorination products. (a) HPLC spectra of aromatic chlorination products on  $\alpha\text{-Fe}_2\text{O}_3$  after 2 h of photoelectrolysis. (b-e) The external standard curves of acetanilide and chlorination products.

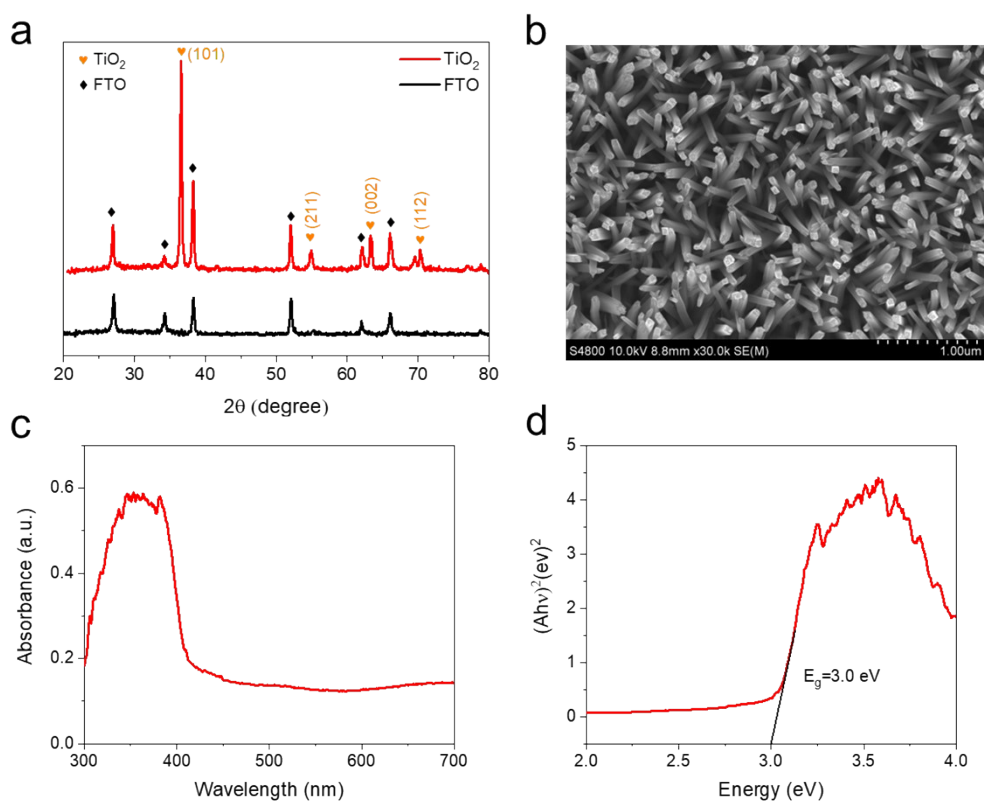


**Fig. S14.** Structural characterizations of TiO<sub>2</sub>. (a) XRD and (b) SEM image of an TiO<sub>2</sub> photoanode. (c) UV-vis spectrum and (d) the corresponding Tauc plot of an TiO<sub>2</sub> photoanode.

XRD showed that TiO<sub>2</sub> displayed a typical rutile phase of TiO<sub>2</sub>. The SEM image of TiO<sub>2</sub> photoanodes indicated that the as-prepared TiO<sub>2</sub> film consisted of nanorod array structure. UV-vis spectrum showed the UV light absorption of the as-prepared sample. And the corresponding Tauc plot gave an optical band gap of 3.0 eV. These results are consistent with those reported in the literature and confirm the successful fabrication of TiO<sub>2</sub> photoanodes.<sup>8, 21</sup>

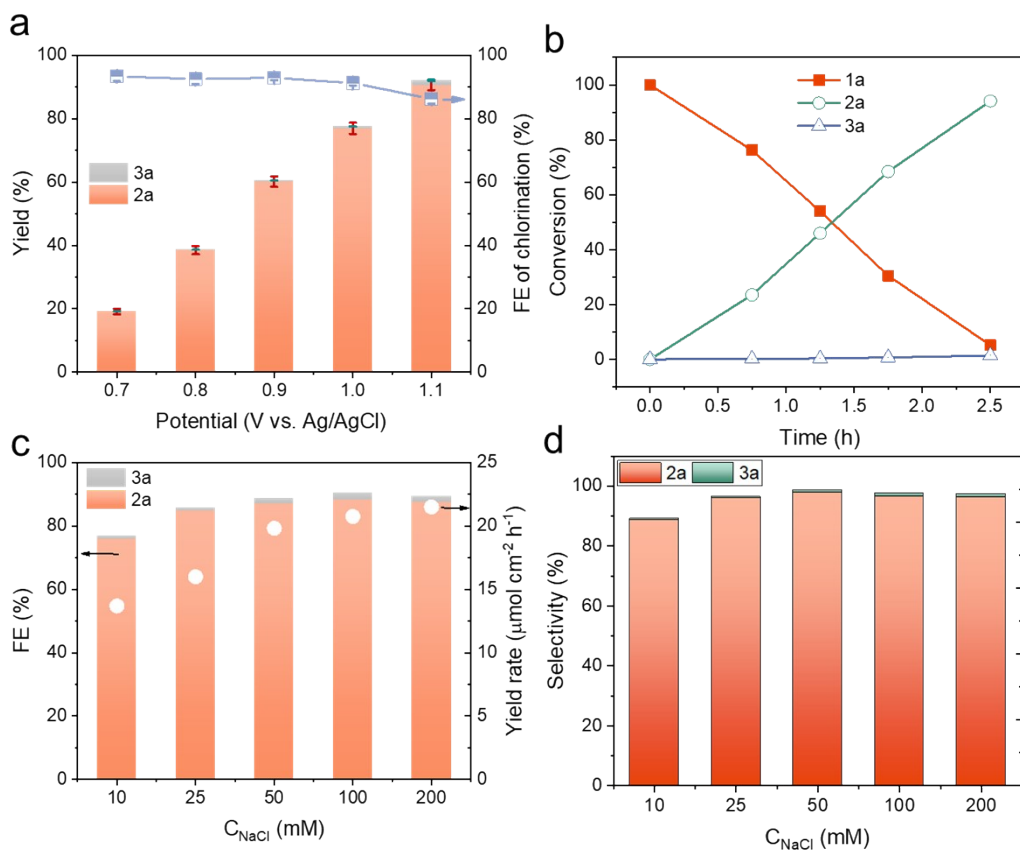


**Fig. S15.** Photoelectrolysis experiments of aromatic chlorination on  $\alpha\text{-Fe}_2\text{O}_3$ . (a) Potential-dependent conversions of **1a** to **2a** and **3a** in 0.1 M NaCl solution. (b) Time-dependent conversions of **1a** to **2a** and **3a** in 0.1 M NaCl solution. (c) Cl-dependent conversions of **1a** to **2a** and **3a**. (d) The selectivity as a function of  $\text{Cl}^-$  concentrations after 2 h photoelectrolysis at 1.0 V vs. Ag/AgCl.

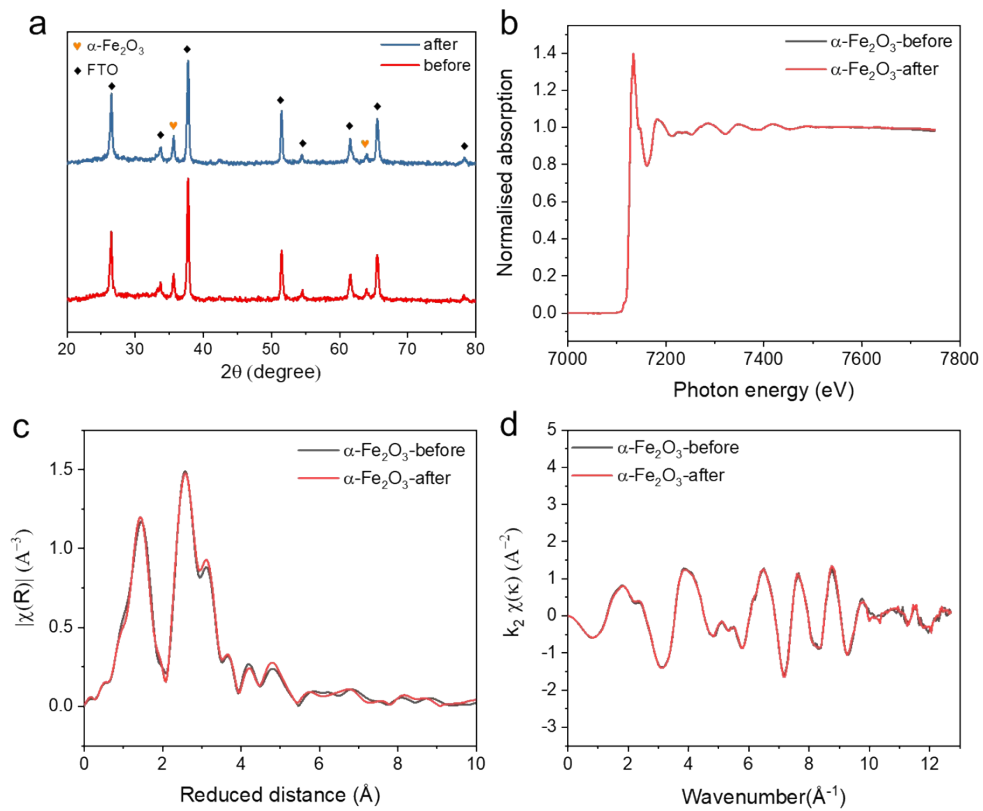


**Fig. S16.** Structural characterizations of  $\alpha$ -Fe<sub>2</sub>O<sub>3</sub> before and after photoelectrolysis. (a) XRD patterns. (b) XAFS spectra of fresh  $\alpha$ -Fe<sub>2</sub>O<sub>3</sub> and used  $\alpha$ -Fe<sub>2</sub>O<sub>3</sub>. (c) EXAFS spectra of at Fe K-edge. (d) The q space spectra at Fe K-edge.

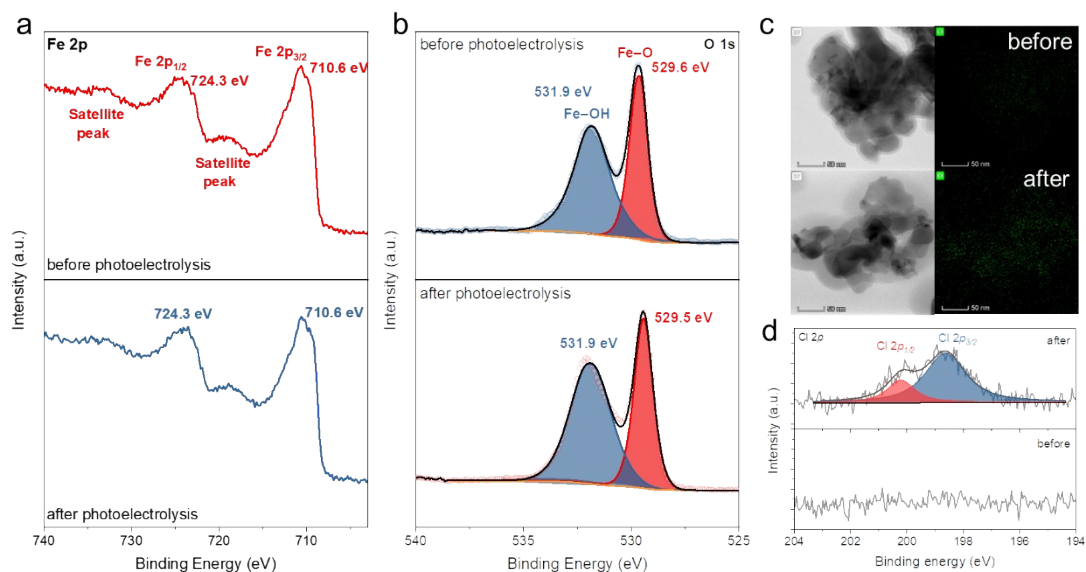


**Fig. S17.** XPS and TEM characterizations of  $\alpha$ -Fe<sub>2</sub>O<sub>3</sub> before and after photoelectrolysis. (a) XPS spectra of the Fe 2p core level and (b) the O 1s core level for  $\alpha$ -Fe<sub>2</sub>O<sub>3</sub>. (c) TEM combined EDS Cl mapping images of  $\alpha$ -Fe<sub>2</sub>O<sub>3</sub> before photoelectrolysis and after photoelectrolysis. (d) XPS spectra of the Cl 2p core level for  $\alpha$ -Fe<sub>2</sub>O<sub>3</sub>.

After 6 h of photoelectrolysis, no obvious change was observed for the binding energy of Fe and O. However, the obvious adsorption of Cl<sup>-</sup> was observed. As shown in **Fig. S17a**, the two peaks at 710.6 and 724.3 eV were attributed to Fe<sup>3+</sup> 2p<sub>3/2</sub> and Fe<sup>3+</sup> 2p<sub>1/2</sub>, accompanied with their satellite peaks. The peak position and shape of the XPS spectra were consistent with typical reports of  $\alpha$ -Fe<sub>2</sub>O<sub>3</sub> phase.<sup>22, 23</sup> The high-resolution XPS spectra of O 1s were deconvoluted into two peaks at 529.6 and 531.9 eV, which were corresponded to the lattice oxygen (Fe–O) and adsorbed Fe–OH groups (**Fig. S17b**). The little difference (~0.1 eV) between the pristine  $\alpha$ -Fe<sub>2</sub>O<sub>3</sub> and the tested  $\alpha$ -

$\text{Fe}_2\text{O}_3$  may originate from the random errors.<sup>24</sup>

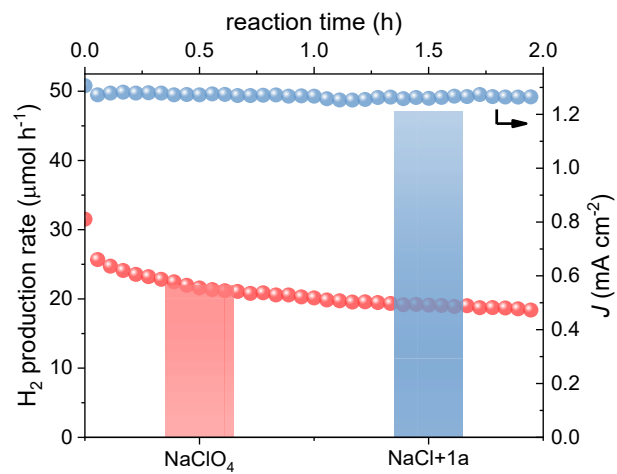


**Fig. S18.** The yield rate of H<sub>2</sub> generation and the photocurrent density on an  $\alpha$ -Fe<sub>2</sub>O<sub>3</sub> photoanode for H<sub>2</sub>O oxidation and electrophilic aromatic chlorination.

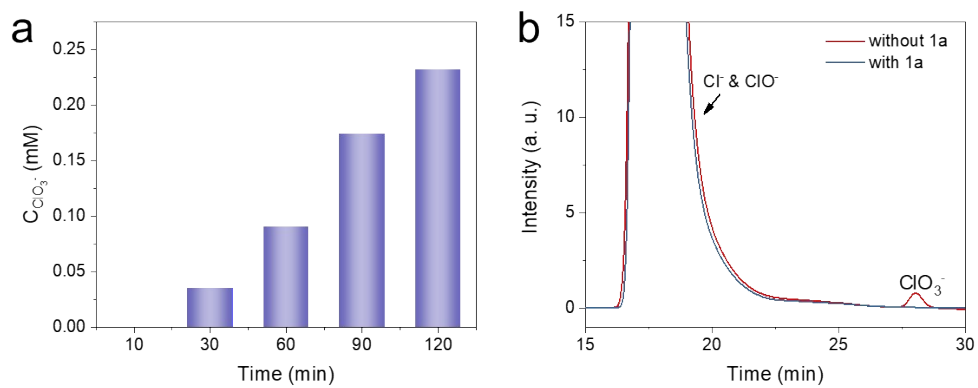


**Fig. S19.** (a) Variations in  $\text{ClO}_3^-$  concentrations over time. (b) The IC signals of  $\text{Cl}^-$  oxidation on  $\alpha\text{-Fe}_2\text{O}_3$  with or without 1a after 2 h of photoelectrolysis at 1.0 V vs. Ag/AgCl.

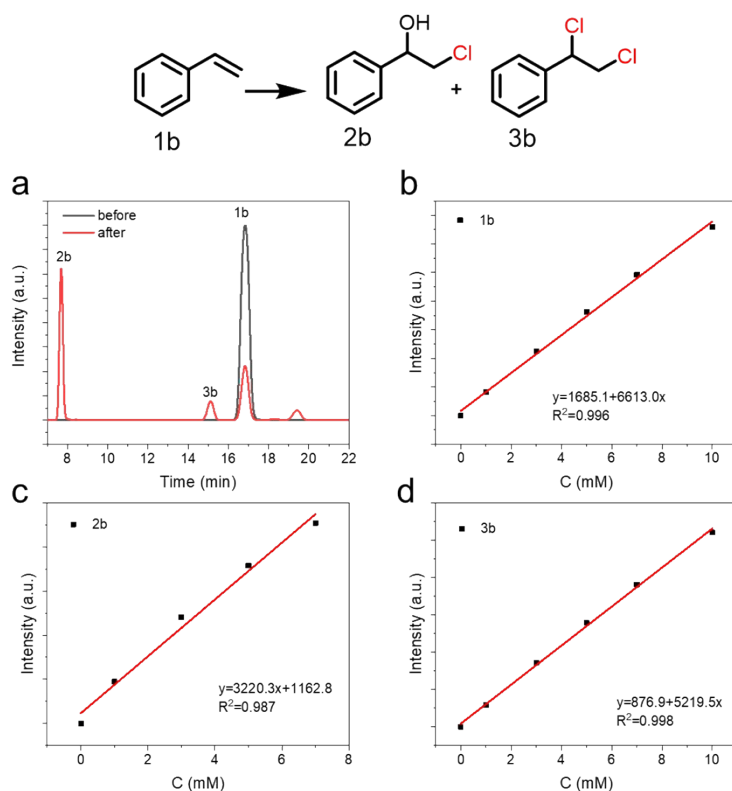


**Fig. S20.** The quantification of alkene chlorination products. (a) HPLC spectra of styrene chlorination products on  $\alpha\text{-Fe}_2\text{O}_3$  after 2 h of photoelectrolysis. (b-d) The external standard curves of styrene and chlorination products. Measurements were run on an Agilent LC instrument with a C18 column and DAD detector. Detection wavelength was 216 nm and mobile phase ratio was 30%  $\text{H}_2\text{O}$  : 70%  $\text{CH}_3\text{CN}$ .

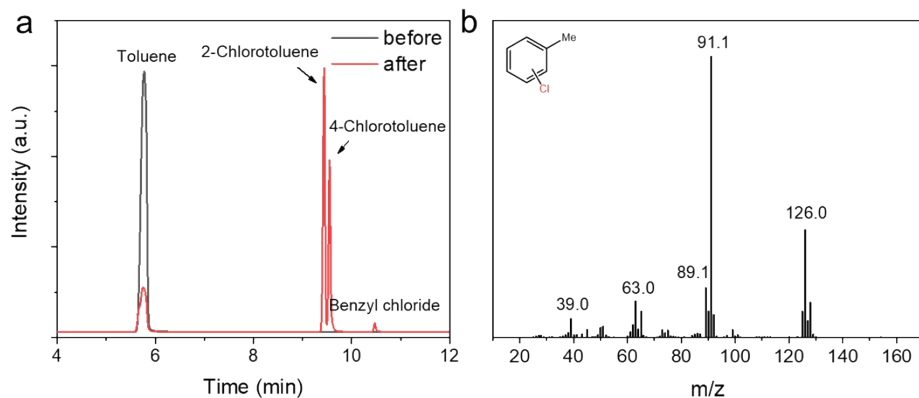


**Fig. S21.** PEC aromatic chlorination of toluene. (a) GC spectrum of the products of PEC aromatic chlorination of toluene (compound **2**) on  $\alpha$ - $\text{Fe}_2\text{O}_3$  photoanode in 0.1 M NaCl electrolyte (50%  $\text{H}_2\text{O}$ , 50% MeCN) with 0.1 mmol toluene at 1.0 V vs. Ag/AgCl under AM 1.5G,  $100 \text{ mW cm}^{-2}$  irradiation for 2 h. (b) The MS spectra of aromatic chlorination products.

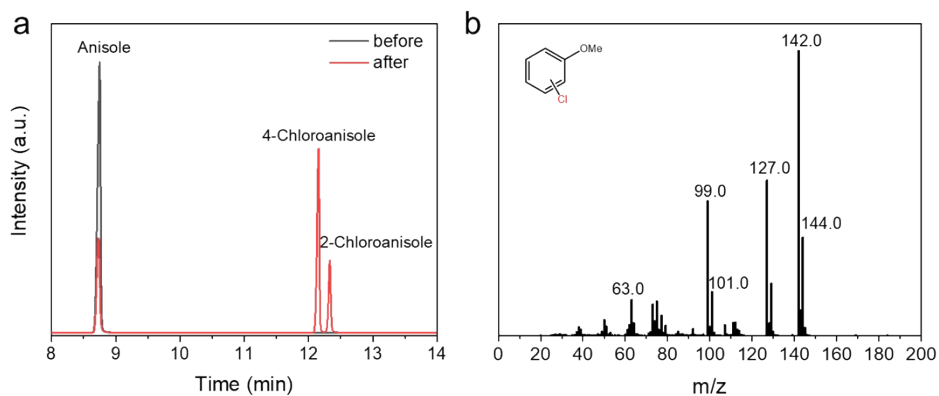


**Fig. S22.** PEC aromatic chlorination of anisole. (a) GC spectrum of the products of PEC aromatic chlorination of anisole (compound **3**) on the  $\alpha$ - $\text{Fe}_2\text{O}_3$  photoanode in 0.1 M NaCl electrolyte (50%  $\text{H}_2\text{O}$ , 50% MeCN) with 0.1 mmol anisole at 1.0 V vs. Ag/AgCl under AM 1.5G,  $100 \text{ mW cm}^{-2}$  irradiation for 2 h. (b) The MS spectra of aromatic chlorination products.

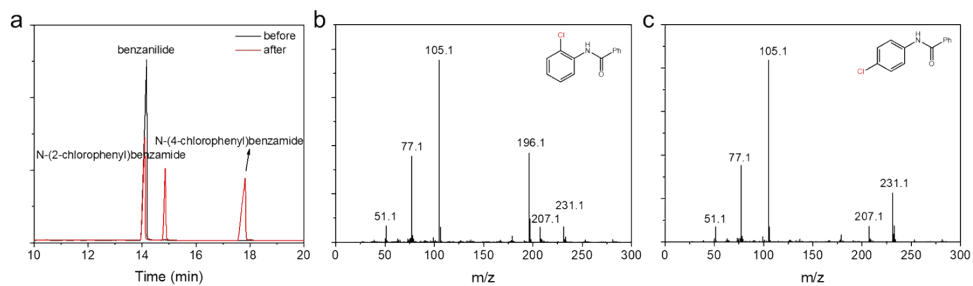


**Fig. S23.** PEC aromatic chlorination of benzanilide. (a) GC spectrum of the products of PEC aromatic chlorination of benzanilide (compound **4**) on the  $\alpha$ -Fe<sub>2</sub>O<sub>3</sub> photoanode in 0.1 M NaCl electrolyte (50% H<sub>2</sub>O, 50% MeCN) with 0.1 mmol benzanilide at 1.0 V vs. Ag/AgCl under AM 1.5G, 100 mW cm<sup>-2</sup> irradiation for 2 h. (b) The MS spectra of aromatic chlorination products.

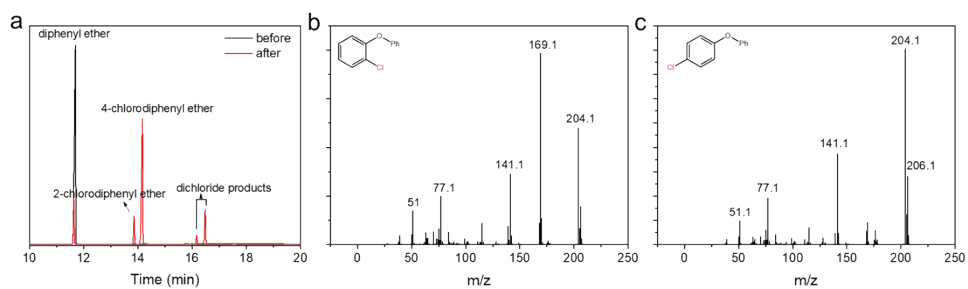


**Fig. S24.** PEC aromatic chlorination of diphenyl ether. (a) GC spectrum of the products of PEC aromatic chlorination of diphenyl ether (compound **5**) on the  $\alpha\text{-Fe}_2\text{O}_3$  photoanode in 0.1 M NaCl electrolyte (16%  $\text{H}_2\text{O}$ , 84% MeCN) with 0.1 mmol diphenyl ether at 1.0 V vs. Ag/AgCl under AM 1.5G,  $100 \text{ mW cm}^{-2}$  irradiation for 2 h. (b) The MS spectra of aromatic chlorination products.

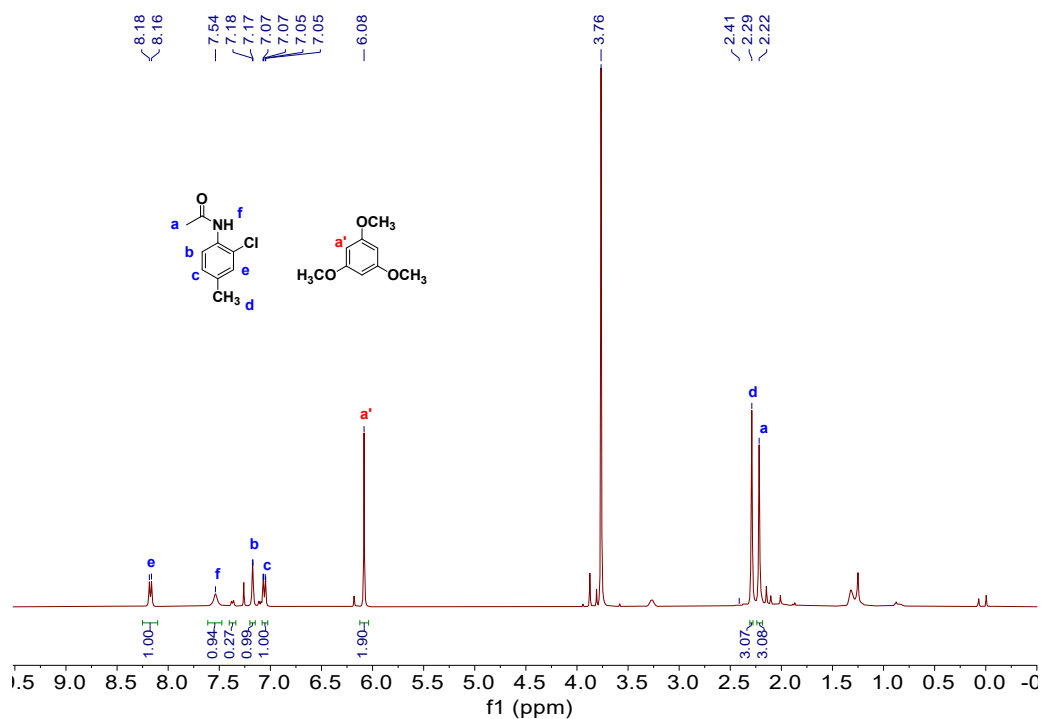


**Fig. S25.** <sup>1</sup>H NMR spectrum of the products of PEC aromatic chlorination of N-methyl-N-(4-methylphenyl)acetamide (compound 7) in 0.1 M NEtBF<sub>4</sub> electrolyte (16% H<sub>2</sub>O, 84% MeCN) with 0.1 mmol N-methyl-N-(4-methylphenyl)acetamide and 50 mM NaCl at 1.0 V vs. Ag/AgCl under AM 1.5G, 100 mW cm<sup>-2</sup> irradiation for 5 h.

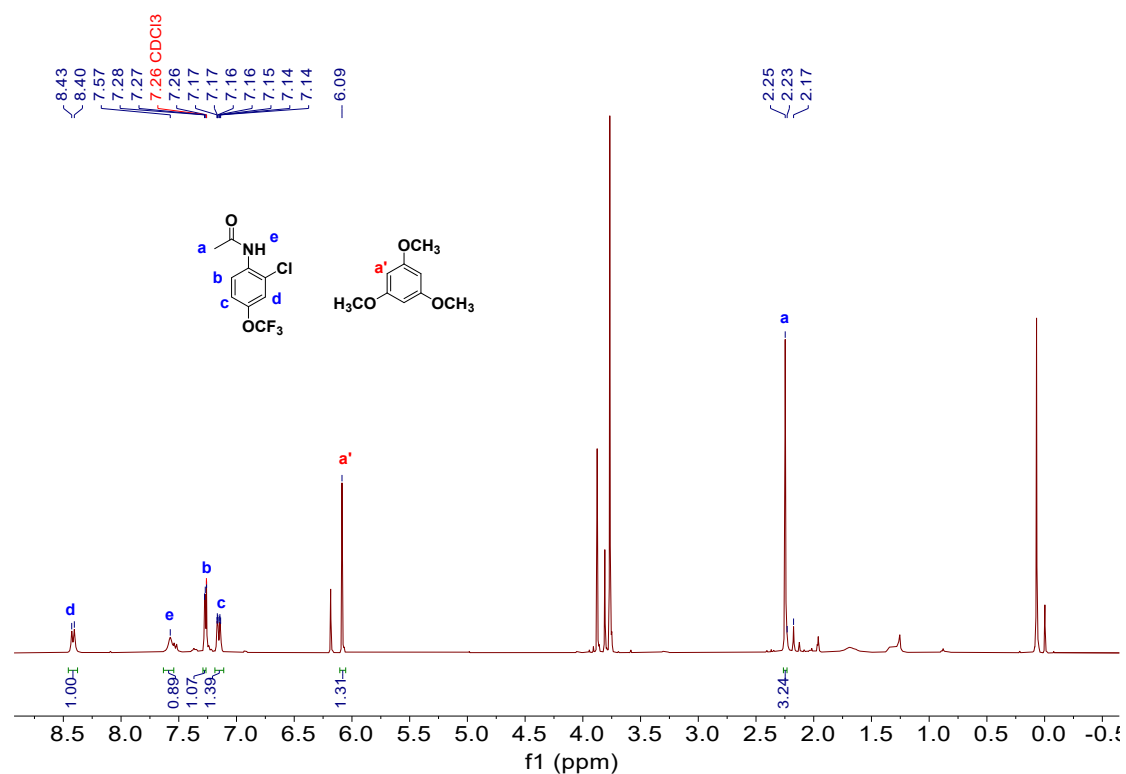


**Fig. S26.** <sup>1</sup>H NMR spectrum of the products of PEC aromatic chlorination of 4-(trifluoromethoxy)acetanilide (compound **8**) in 0.1 M NEtBF<sub>4</sub> electrolyte (16% H<sub>2</sub>O, 84% MeCN) with 0.1 mmol 4-(trifluoromethoxy)acetanilide and 50 mM NaCl at 1.0 V vs. Ag/AgCl under AM 1.5G, 100 mW cm<sup>-2</sup> irradiation for 5 h.

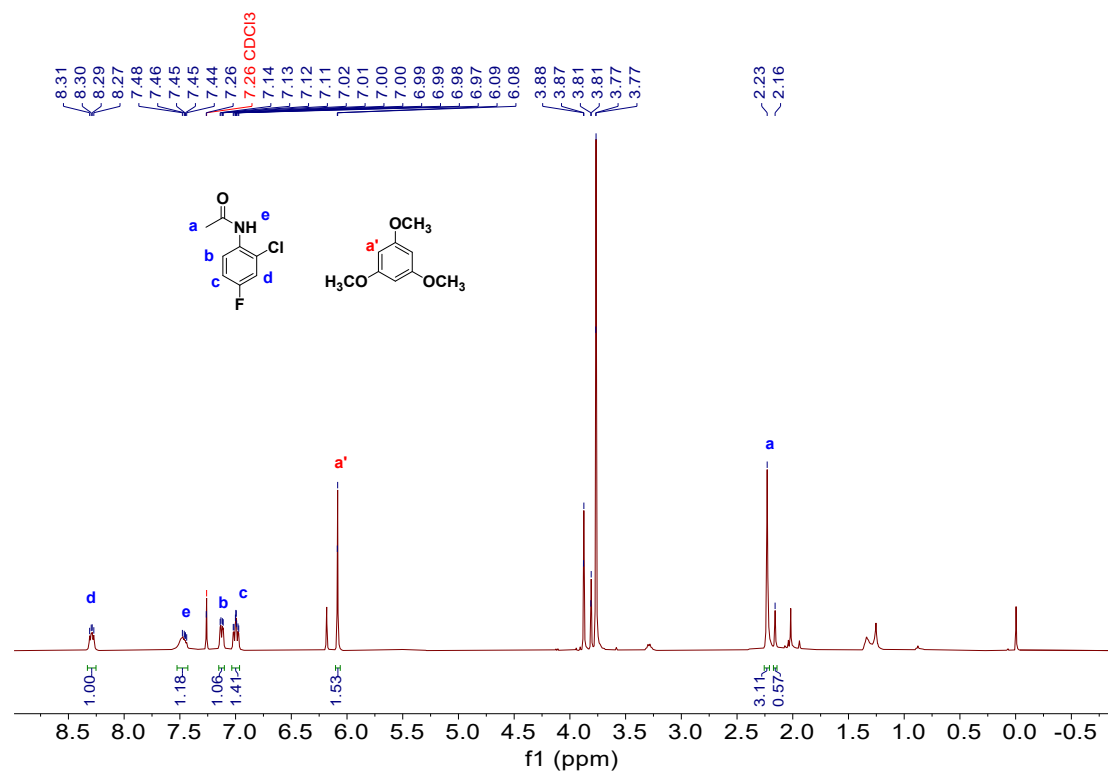


**Fig. S27.**  $^1\text{H}$  NMR spectrum of the products of PEC aromatic chlorination of 4-fluoroacetanilide (compound **9**) in 0.1 M  $\text{NEt}_4\text{BF}_4$  electrolyte (16%  $\text{H}_2\text{O}$ , 84% MeCN) with 0.1 mmol 4-fluoroacetanilide and 50 mM NaCl at 1.0 V vs. Ag/AgCl under AM 1.5G,  $100 \text{ mW cm}^{-2}$  irradiation for 5 h.

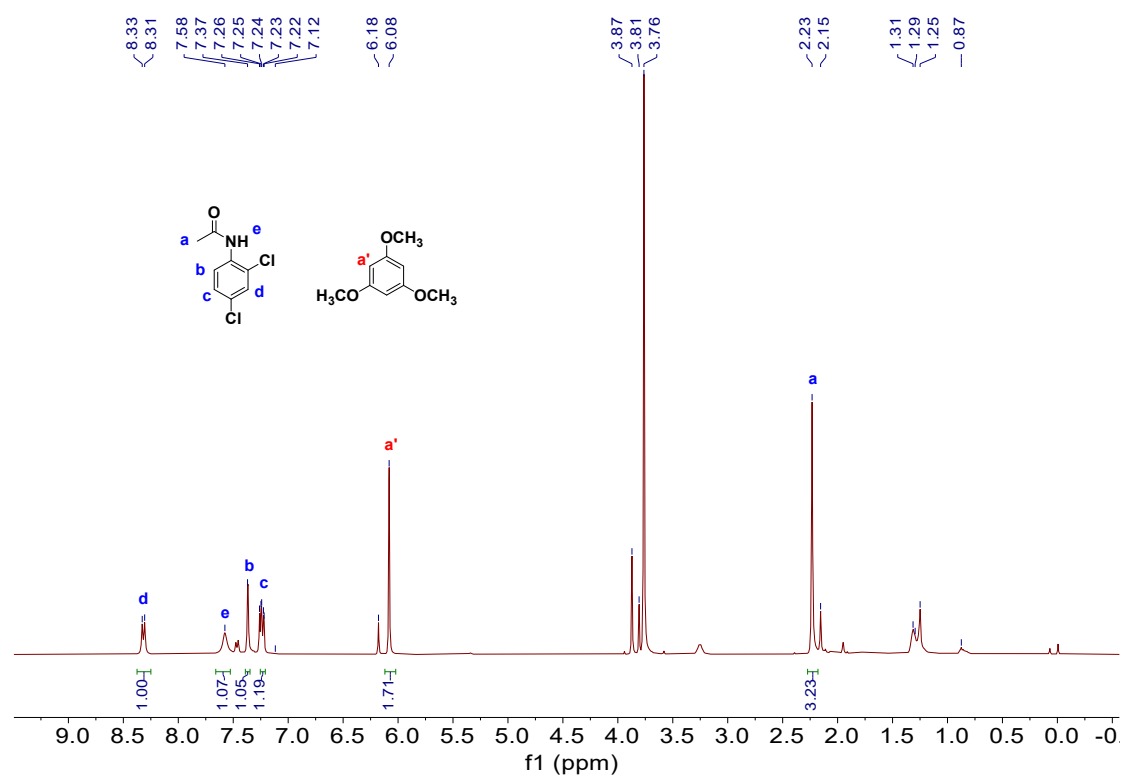


**Fig. S28.** <sup>1</sup>H NMR spectrum of the products of PEC aromatic chlorination of 4-chloroacetanilide (compound **10**) in 0.1 M NEtBF<sub>4</sub> electrolyte (16% H<sub>2</sub>O, 84% MeCN) with 0.1 mmol 4-chloroacetanilide and 50 mM NaCl at 1.0 V vs. Ag/AgCl under AM 1.5G, 100 mW cm<sup>-2</sup> irradiation for 5 h.

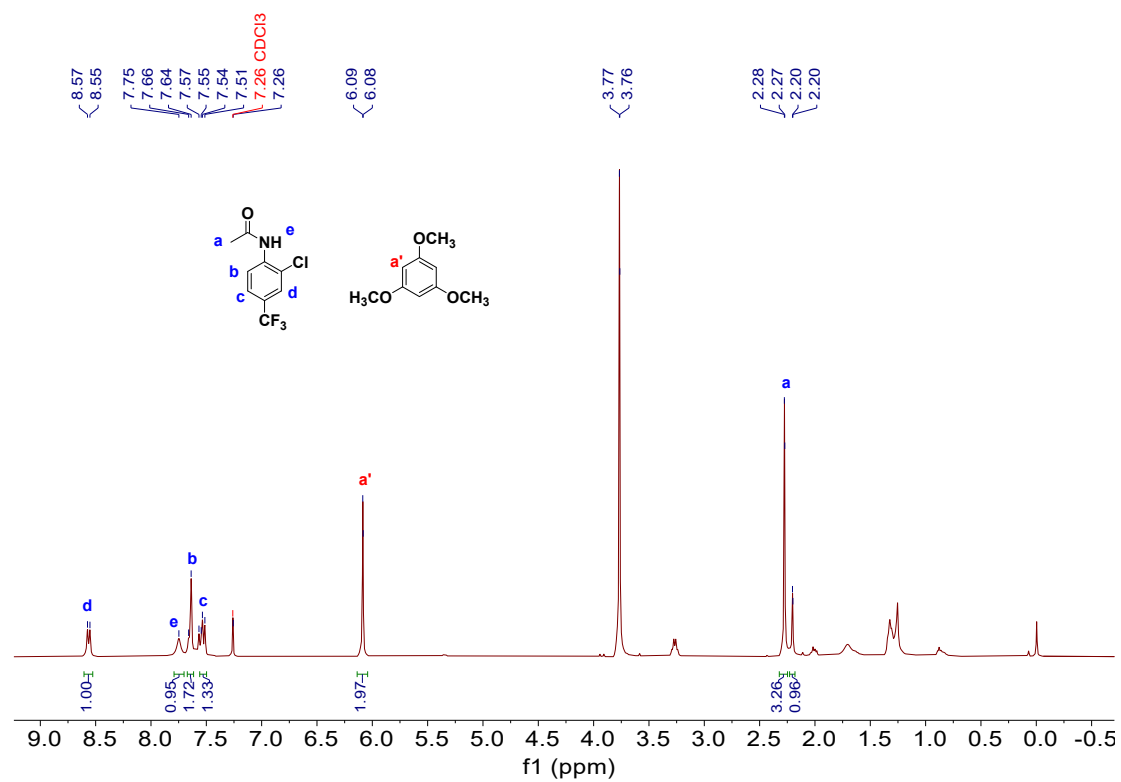


**Fig. S29.** <sup>1</sup>H NMR spectrum of the products of PEC aromatic chlorination of 4-(trifluoromethyl)acetanilide (compound **11**) in 0.1 M NEtBF<sub>4</sub> electrolyte (16% H<sub>2</sub>O, 84% MeCN) with 0.1 mmol 4-(trifluoromethyl)acetanilide and 50 mM NaCl at 1.0 V vs. Ag/AgCl under AM 1.5G, 100 mW cm<sup>-2</sup> irradiation for 5 h.

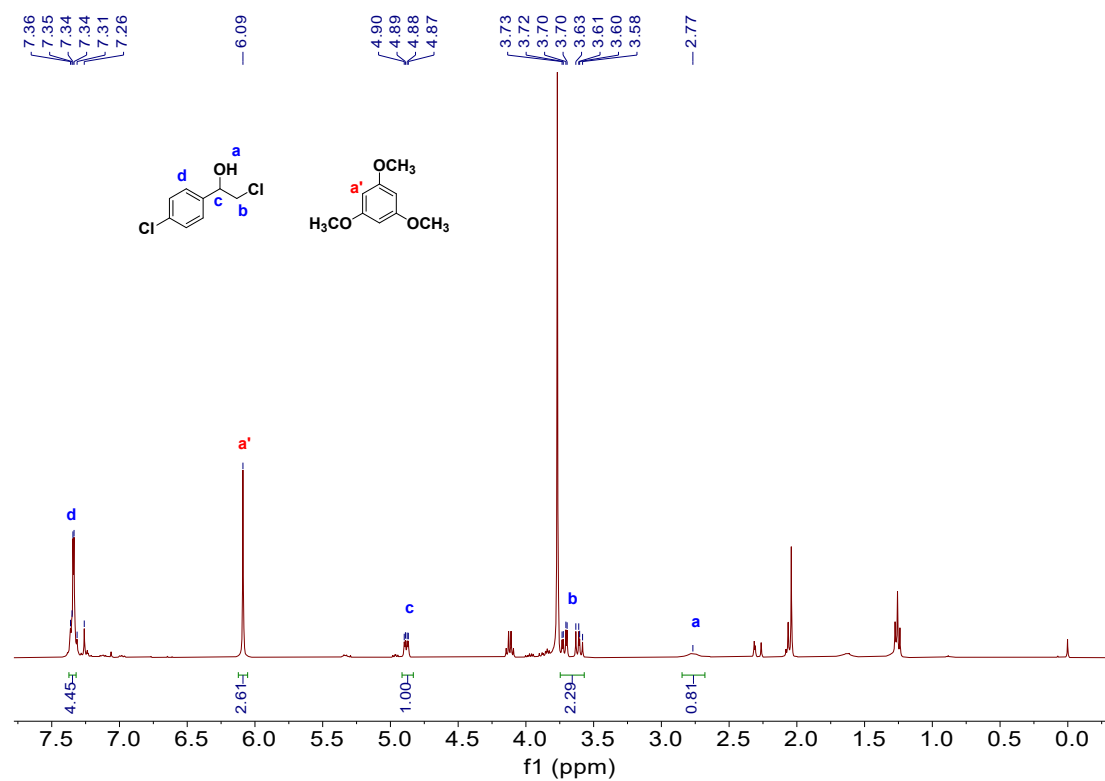


**Fig. S30.** <sup>1</sup>H NMR spectrum of the products of PEC chlorohydration of 4-chlorostyrene (compound **13**) in 0.1 M NaCl electrolyte (50% H<sub>2</sub>O, 50% MeCN) with 0.1 mmol 4-chlorostyrene at 1.0 V vs. Ag/AgCl under AM 1.5G, 100 mW cm<sup>-2</sup> irradiation for 2 h.

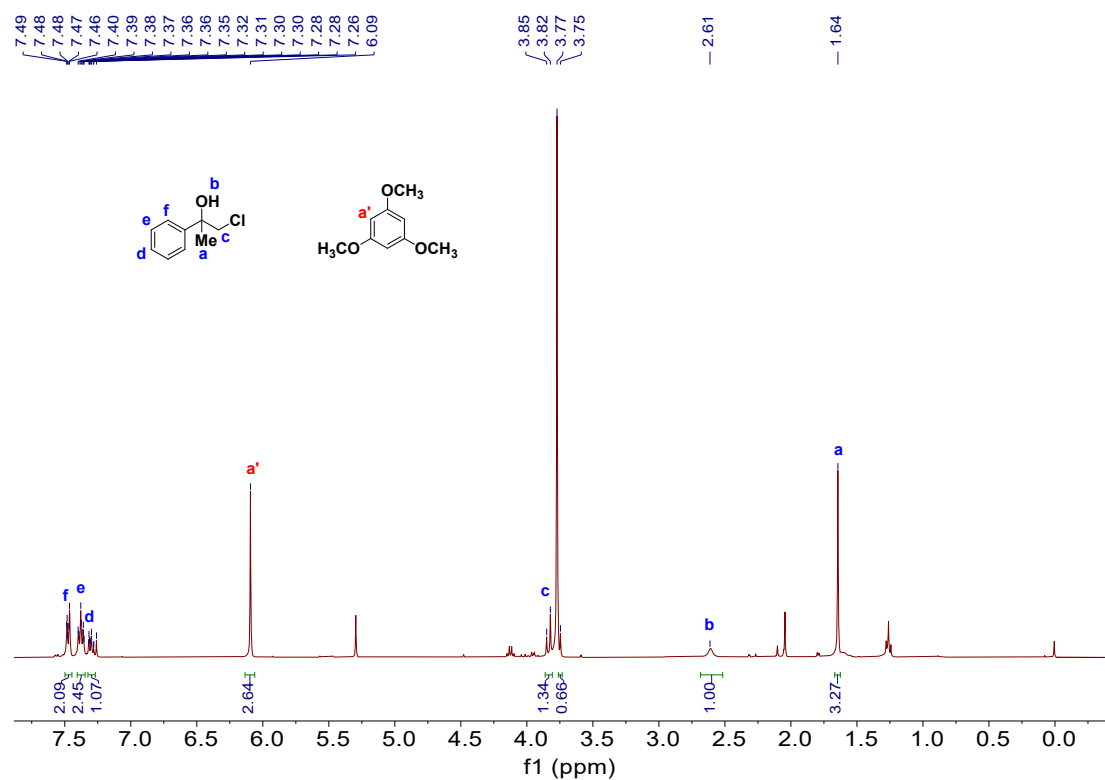


**Fig. S31.** <sup>1</sup>H NMR spectrum of the products of PEC chlorohydration of 2-phenyl-1-propene (compound **14**) in 0.1 M NaCl electrolyte (50% H<sub>2</sub>O, 50% MeCN) with 0.1 mmol 2-phenyl-1-propene at 1.0 V vs. Ag/AgCl under AM 1.5G, 100 mW cm<sup>-2</sup> irradiation for 2 h.

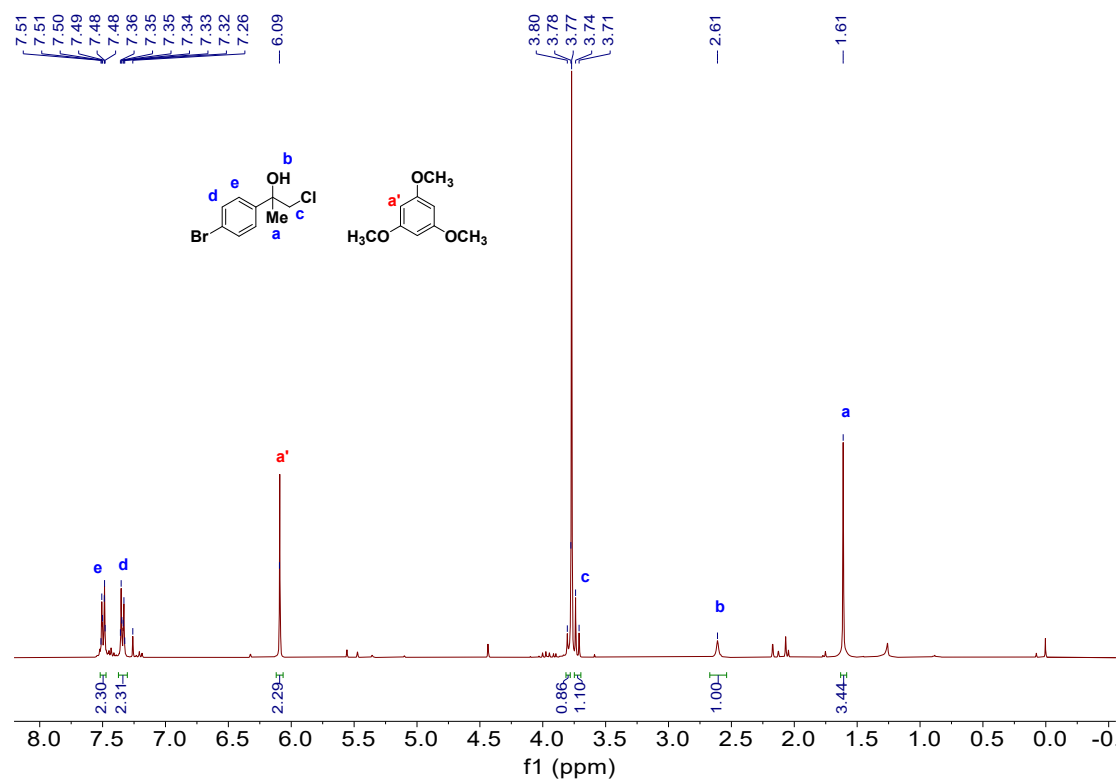


**Fig. S32.** <sup>1</sup>H NMR spectrum of the products of PEC chlorohydration of 1-bromo-4-(1-methylethenyl)benzene (compound **15**) in 0.1 M NaCl electrolyte (50% H<sub>2</sub>O, 50% MeCN) with 0.1 mmol 1-bromo-4-(1-methylethenyl)benzene at 1.0 V vs. Ag/AgCl under AM 1.5G, 100 mW cm<sup>-2</sup> irradiation for 2 h.

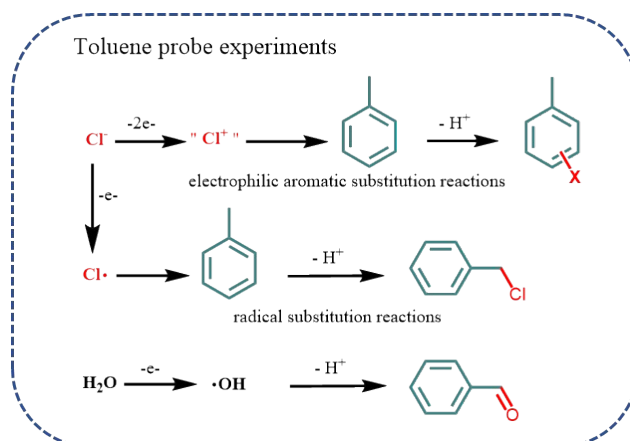


**Fig. S33.** Scheme of the products formed during toluene chlorination when reacting with various active chlorine species.

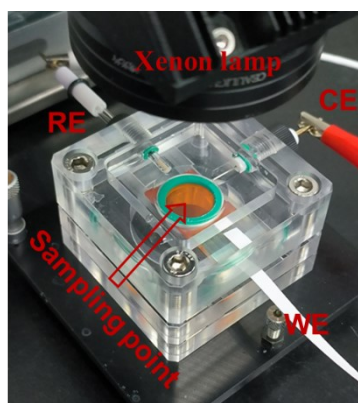


**Fig. S34.** The optical image of the open-type cell used in EPR measurements.

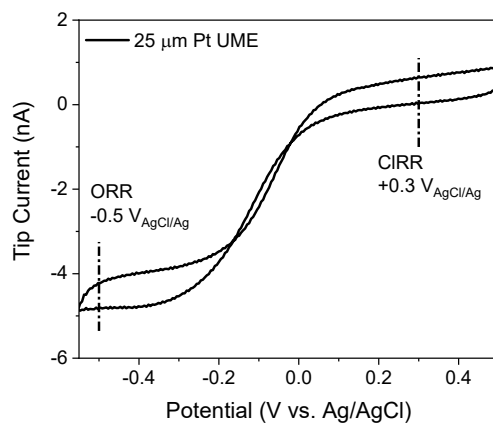


**Fig. S35.** CV curves of UME measured in 0.1 M NaClO<sub>4</sub> with a scan rate of 20 mV s<sup>-1</sup>.

The negative current was originated from the reduction of dissolved oxygen (ORR). The formed Cl<sub>2</sub> was monitored by applying a potential of 0.3 V vs. Ag/AgCl to the tip electrode for the Cl<sub>2</sub> reduction reaction (ClRR). At this potential, neither O<sub>2</sub> nor the formed active chlorine species (e.g., HClO or ClO<sup>-</sup>) were detected due to the sluggish reduction reactions on Pt.<sup>9</sup>

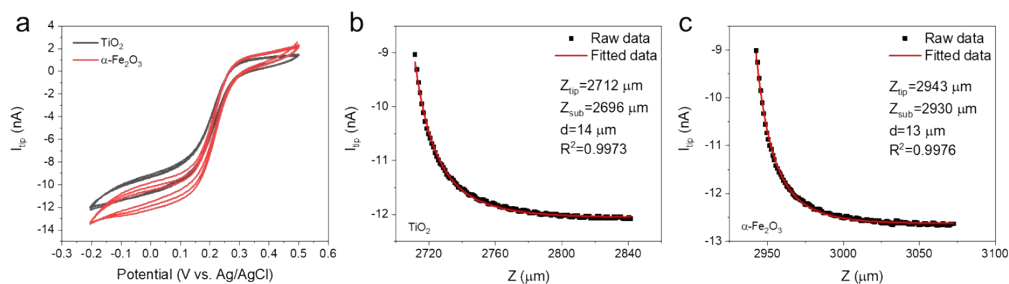


**Fig. S36.** SECM experiments. (a) CV curves of UME measured in a 0.1 M KCl solution containing 5 mM K[Fe(CN)<sub>6</sub>] as the redox mediator. The negative feedback approach curves of the tip electrode for (b) TiO<sub>2</sub> and (c) α-Fe<sub>2</sub>O<sub>3</sub> were measured under dark conditions.

The cut off value of the approach curve was 80%. By fitting the experimental data to the theoretical equations, we determined that the distance between the tip and substrate (referred to as d) when the tip stopped was approximately 13 μm for both α-Fe<sub>2</sub>O<sub>3</sub> and TiO<sub>2</sub>. Therefore, the formation of Cl<sub>2</sub> on the two photoanodes can be directly compared by SECM experiments.

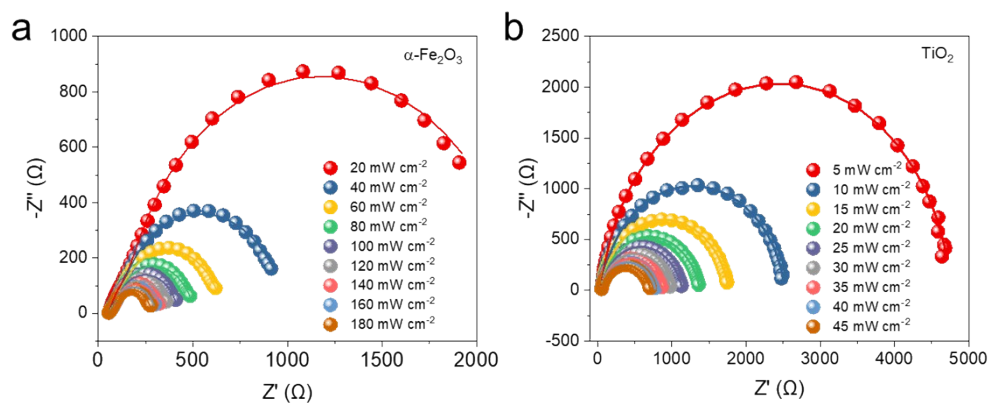


**Fig. S37.** EIS data of (a)  $\alpha\text{-Fe}_2\text{O}_3$  and (b)  $\text{TiO}_2$  photoanodes for  $\text{Cl}^-$  oxidation. The EIS data were measured at the bias of 0.6 and 0.2 V vs. Ag/AgCl for the  $\alpha\text{-Fe}_2\text{O}_3$  and  $\text{TiO}_2$  photoanodes, respectively.

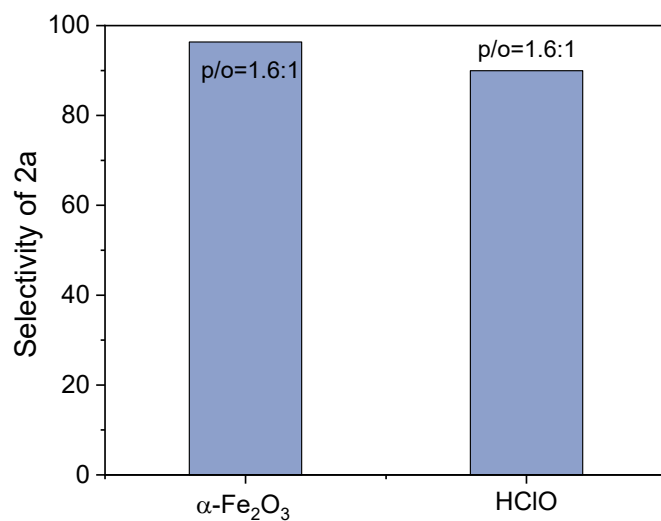


**Fig. S38.** Comparison of PEC aromatic chlorination and HClO mediated aromatic chlorination.

Chlorination products were detected after 1 h of photoelectrolysis at 1.0 V vs. Ag/AgCl for PEC chlorination. In the case of aromatic chlorination by using HClO as the chlorinating reagent, the chlorination products were detected by HPLC after a reaction with 0.1 mmol **1a** and 2 eq HClO at pH=4 in a 10 mL solution (50% H<sub>2</sub>O, 50% MeCN) for 1 h.

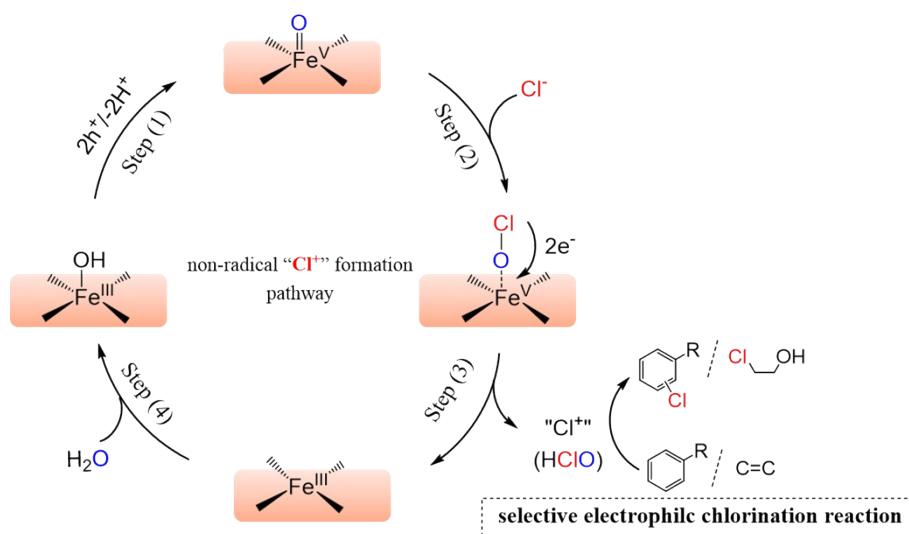


**Fig. S39. The additional proposed mechanisms.**

Considering that the rate-determining step (RDS) involved two surface-trapped holes, there was also a possibility of the formation of an isolated  $\text{Fe}^{\text{V}}=\text{O}$  species for the non-radical Cl activation process. However, it has been reported that the  $\text{Fe}^{\text{V}}=\text{O}$  species were primarily involved in the rate-determining step of water oxidation on  $\alpha\text{-Fe}_2\text{O}_3$ , which involved a three-electron transfer (with a reaction order of 3).<sup>25-27</sup> In this process, two adjacent  $\text{Fe}^{\text{IV}}=\text{O}$  species were firstly formed by the two-hole oxidation of two neighboring surface Fe sites. Subsequently, the third hole oxidized one of the  $\text{Fe}^{\text{IV}}=\text{O}$  groups to form  $\text{Fe}^{\text{V}}=\text{O}$ , providing sufficient oxidation power for water oxidation. This suggested that the accumulation of two adjacent  $\text{Fe}^{\text{IV}}=\text{O}$  species was prior to the formation of  $\text{Fe}^{\text{V}}=\text{O}$  species. Additionally, previous studies have observed that iron-oxo species with a reaction order of 1 and 2 exhibited similar lifetimes, indicating that the nature of iron-oxo species remained unchanged in both cases. The transition in reaction orders was attributed to the varied accumulation states of high-value iron-oxo species.<sup>28</sup> In our study, the EIS analysis suggested that  $\text{Cl}^-$  oxidation was more

favorably mediated by the high-valent iron-oxo species formed on  $\alpha$ -Fe<sub>2</sub>O<sub>3</sub> than H<sub>2</sub>O oxidation (**Fig. 1c and f**). As a result, we are more inclined towards the formation of two adjacent Fe<sup>IV</sup>=O species than the isolated Fe<sup>V</sup>=O species.

**Table S1.** The calculations of FEs( $O_2$ ).

$C_{NaCl}$ (mM)	Q (C)	$A_{O_2}$	$A_{N_2}$	FE( $O_2$ )
0	4.83	194537	50149	97.6%
10	7.90	52779	30060	14.5%
25	8.10	21682	32687	3.8%
50	8.14	16142	29077	2.3%
100	8.51	18056	46211	1.2%
200	10.12	18071	38371	1.6%

There are some systematic errors. (1) To determine the moles of standard gas, we assumed that  $O_2$  standard gas and  $N_2$  standard gas were the ideal gas. (2) The ratio between the leaked  $N_2$  and leaked  $O_2$  was assumed to be equal to that in the air (i.e., 3.7) to exclude the extra oxygen from the air leakage. These systematic errors and random errors resulted in the FE( $O_2$ ) being less than 100%.

**Table S2.** Summary of recent PEC studies on the selectivity of Cl<sup>-</sup> oxidation to active chlorine.

Entry	Photoanode	Electrolyte	Light sources	bias	FE	Ref.
1	$\alpha$ -Fe <sub>2</sub> O <sub>3</sub>	50 mM NaCl (pH 6.4)	1 sun <sup>a</sup>	1.0 V (vs. Ag/AgCl).	92%	This work
2	WO <sub>3</sub>	0.5 M NaCl (pH 2.5)	1 sun	0.9 V (vs. Ag/AgCl)	~70%	1 <sup>29</sup>
3	WO <sub>3</sub> :B	0.5 M NaCl (pH 2)	1 sun	1.23 V (vs. RHE)	~25%	2 <sup>30</sup>
4	WO <sub>3</sub>	Seawater (pH 6.4)	1 sun	1.23 V (vs. RHE)	~56%	3 <sup>31</sup>
5	BiVO <sub>4</sub> @WO <sub>3</sub>	4 M NaCl (pH 1)	1 sun	1.42 V (vs. RHE)	~74%	4 <sup>32</sup>
6	WO <sub>3</sub> @ BiVO <sub>4</sub>	5 M NaCl (neutral)	1 sun	0.22 (vs. Pt CE)	~80%	5 <sup>33</sup>
7	WO <sub>3</sub> @ BiVO <sub>4</sub> @CoO <sub>x</sub>	0.5 M NaCl (pH 5.9)	1 sun	1 V (vs. RHE)	~100%	6 <sup>34</sup>
8	BiVO <sub>4</sub> :Mo@R hO <sub>2</sub>	Seawater (pH 6)	1 sun	1 V (vs. RHE)	~25%	7 <sup>35</sup>

<sup>a</sup>1 sun: AM 1.5 G (100 mW cm<sup>-2</sup>)

**Table S3.** Electrochemical parameters fitted from EIS data for water oxidation.

<b>Potential</b> <b>(V vs. Ag/AgCl)</b>	<b>C<sub>trap</sub></b> <b>(<math>\mu</math>F)</b>	<b>R<sub>s</sub></b> <b>(<math>\Omega</math>)</b>	<b>R<sub>trapping</sub></b> <b>(<math>\Omega</math>)</b>	<b>R<sub>ct,trap</sub></b> <b>(<math>\Omega</math>)</b>
0.40	87.7	55.7	35.9	98249.0
0.45	100.7	56.2	55.1	94964.0
0.50	146.0	56.3	56.9	38724.0
0.55	210.9	56.2	53.1	10406.0
0.60	275.2	55.9	51.2	3295.8
0.65	326.9	55.6	51.4	1288.2
0.70	386.1	55.0	52.6	634.8
0.75	487.1	54.7	52.5	365.6
0.80	606.7	55.1	52.0	238.6
0.85	647.4	55.5	55.6	178.1
0.90	599.0	55.7	65.0	152.2
0.95	490.3	56.0	82.8	150.3
1.00	360.2	56.2	115.7	170.1
1.05	242.0	56.4	175.1	218.8
1.10	149.8	56.6	282.3	302.1

Reaction conditions: 0.1 M NaClO<sub>4</sub>, 50% H<sub>2</sub>O in 15 mL of CH<sub>3</sub>CN solution, under 470nm LED irradiation.

**Table S4.** Electrochemical parameters fitted from EIS data for Cl<sup>-</sup> oxidation.

<b>Potential</b> <b>(V vs. Ag/AgCl)</b>	<b>C<sub>trap</sub></b> <b>(<math>\mu</math>F)</b>	<b>R<sub>s</sub></b> <b>(<math>\Omega</math>)</b>	<b>R<sub>trapping</sub></b> <b>(<math>\Omega</math>)</b>	<b>R<sub>ct,trap</sub></b> <b>(<math>\Omega</math>)</b>
0.40	283.6	58.7	46.3	7461.2
0.45	274.7	58.5	46.9	3844.8
0.50	278.4	58.2	47.5	1690.4
0.55	301.2	57.9	48.8	753.1
0.60	325.2	57.6	51.4	379.9
0.65	350.3	57.3	54.2	223.9
0.70	382.5	57.2	56.3	152.7
0.75	416.2	57.2	58.0	118.4
0.80	438.6	57.5	60.6	102.4
0.85	452.8	57.9	65.3	96.3
0.90	427.5	58.2	76.0	95.7
0.95	388.9	58.6	94.1	103.2
1.00	321.0	58.9	127.6	120.3
1.05	249.1	59.1	189.9	152.6
1.10	179.0	59.3	295.0	216.4

Reaction conditions: 10 mM NaCl, 90 mM NaClO<sub>4</sub>, 50% H<sub>2</sub>O in 15 mL of CH<sub>3</sub>CN solution, under 470nm LED irradiation.

**Table S5.** The detailed data of fitted EIS for a  $\alpha$ -Fe<sub>2</sub>O<sub>3</sub> photoanode.

Light Intensity (mW cm <sup>-2</sup> )	J ( $\mu$ A cm <sup>-2</sup> )	C <sub>trap</sub> ( $\mu$ F)	R <sub>s</sub> ( $\Omega$ )	R <sub>trapping</sub> ( $\Omega$ )	R <sub>ct,trap</sub> ( $\Omega$ )
20	10.0	83.7	57.2	464.6	1764.4
40	23.2	139.4	56.8	162.2	784.7
60	35.9	182.2	56.4	96.7	508.7
80	46.9	209.5	56.1	71.3	382.8
100	56.5	228.4	55.7	57.6	313.0
120	66.3	240.6	55.4	49.3	267.4
140	74.7	268.6	55.2	41.2	236.4
160	81.8	277.9	55.0	36.9	213.1
180	88.6	284.6	54.7	33.7	195.0

Reaction conditions: 0.1 M NaCl, 50% H<sub>2</sub>O in 15 mL of CH<sub>3</sub>CN solution, reaction at 0.6 V vs. Ag/AgCl under 470 nm LED irradiation.

**Table S6.** The detailed data of fitted EIS for a TiO<sub>2</sub> photoanode.

Light Intensity (mW cm <sup>-2</sup> )	J (μA cm <sup>-2</sup> )	C <sub>trap</sub> (μF)	R <sub>s</sub> (Ω)	R <sub>trapping</sub> (Ω)	R <sub>ct,trap</sub> (Ω)
5	26.5	178.0	53.6	4318.5	391.5
10	46.0	428.5	53.1	2285	181.8
15	63.6	502.7	52.9	1553.5	157.8
20	80.0	553.7	52.6	1176	150.9
25	95.7	614.5	52.2	962.4	129.2
30	110.5	663.3	51.9	815.0	117.9
35	124.8	589.9	51.7	694.5	123.5
40	138.4	599.6	51.4	617.1	112.3
45	151.4	601.2	51.1	555.9	107.3

Reaction conditions: 0.1 M NaCl, 50% H<sub>2</sub>O in 15 mL of CH<sub>3</sub>CN solution, reaction at 0.2 V vs. Ag/AgCl under 365 nm LED irradiation.

## Reference

1. L. Wu, D. Tang, J. Xue, S. Liu, J. Wang, H. Ji, C. Chen, Y. Zhang and J. Zhao, Competitive non-radical nucleophilic attack pathways for NH<sub>3</sub> oxidation and H<sub>2</sub>O oxidation on hematite photoanodes, *Angew. Chem. Int. Ed.*, 2022, **61**, e202214580.
2. J. Xue, L. Wu, C. Deng, D. Tang, S. Wang, H. Ji, C. Chen, Y. Zhang and J. Zhao, Plasmon-mediated electrochemical activation of Au/TiO<sub>2</sub> nanostructure-based photoanodes for enhancing water oxidation and antibiotic degradation, *ACS Appl. Nano Mater.*, 2022, **5**, 11342-11351.
3. Y. Yao, L. Zhao, J. Dai, J. Wang, C. Fang, G. Zhan, Q. Zheng, W. Hou and L. Zhang, Single atom Ru monolithic electrode for efficient chlorine evolution and nitrate reduction, *Angew. Chem. Int. Ed.*, 2022, **61**, e202208215.
4. C. Lefrou and R. Cornut, Analytical Expressions for quantitative scanning electrochemical microscopy (SECM), *ChemPhysChem*, 2010, **11**, 547-556.
5. P. Sun, F. O. Laforge and M. V. Mirkin, Scanning electrochemical microscopy in the 21st century, *Phys. Chem. Chem. Phys.*, 2007, **9**, 802-823.
6. S. Chu, W. Li, Y. Yan, T. Hamann, I. Shih, D. Wang and Z. Mi, Roadmap on solar water splitting: current status and future prospects, *Nano Futures*, 2017, **1**, 022001.
7. A. G. Breuhaus-Alvarez, Q. Cheek, J. J. Cooper, S. Maldonado and B. M. Bartlett, Chloride oxidation as an alternative to the oxygen-evolution reaction on H<sub>x</sub>WO<sub>3</sub> Photoelectrodes, *J. Phys. Chem. C*, 2021, **125**, 8543-8550.

8. Z. Li, L. Luo, M. Li, W. Chen, Y. Liu, J. Yang, S.-M. Xu, H. Zhou, L. Ma, M. Xu, X. Kong and H. Duan, Photoelectrocatalytic C–H halogenation over an oxygen vacancy-rich TiO<sub>2</sub> photoanode, *Nat. Commun.*, 2021, **12**, 6698.
9. M. Li, Y. Yang, Y. Ling, W. Qiu, F. Wang, T. Liu, Y. Song, X. Liu, P. A.-O. X. Fang, Y. Tong and Y. A.-O. Li, Morphology and doping engineering of Sn-doped hematite nanowire photoanodes, *Nano Lett.*, 2017, **17**, 2490-2495.
10. C. Wang, X. Long, S. Wei, T. Wang, F. Li, L. Gao, Y. Hu, S. Li and J. Jin, Conformally coupling CoAl-Layered double hydroxides on fluorine-doped hematite: surface and bulk Co-modification for enhanced photoelectrochemical water oxidation, *ACS Appl. Mater. Interfaces*, 2019, **11**, 29799-29806.
11. Q. Guo, Q. Zhao, R. Crespo-Otero, D. Di Tommaso, J. Tang, S. D. Dimitrov, M.-M. Titirici, X. Li and A. B. Jorge Sobrido, Single-atom iridium on hematite photoanodes for solar water splitting: catalyst or spectator?, *J. Am. Chem. Soc.*, 2023, **145**, 1686-1695.
12. T. H. Jeon, G.-h. Moon, H. Park and W. Choi, Ultra-efficient and durable photoelectrochemical water oxidation using elaborately designed hematite nanorod arrays, *Nano Energy*, 2017, **39**, 211-218.
13. J. Y. Kim, D. H. Youn, K. Kang and J. S. Lee, Highly conformal deposition of an ultrathin FeOOH Layer on a hematite nanostructure for efficient solar water splitting, *Angew. Chem. Int. Ed.*, 2016, **55**, 10854-10858.
14. S. Shen, S. A. Lindley, X. Chen and J. Z. Zhang, Hematite heterostructures for photoelectrochemical water splitting: rational materials design and charge

- carrier dynamics, *Energy Environ. Sci.*, 2016, **9**, 2744-2775.
15. C. Jiang, S. J. A. Moniz, A. Wang, T. Zhang and J. Tang, Photoelectrochemical devices for solar water splitting – materials and challenges, *Chem. Soc. Rev.*, 2017, **46**, 4645-4660.
  16. P. Sharma, J.-W. Jang and J. S. Lee, Key Strategies to advance the photoelectrochemical water splitting performance of  $\alpha$ -Fe<sub>2</sub>O<sub>3</sub> Photoanode, *ChemCatChem*, 2019, **11**, 157-179.
  17. B. Klahr, S. Gimenez, F. Fabregat-Santiago, J. Bisquert and T. W. Hamann, Electrochemical and photoelectrochemical investigation of water oxidation with hematite electrodes, *Energy Environ. Sci.*, 2012, **5**, 7626-7636.
  18. B. Klahr, S. Gimenez, F. Fabregat-Santiago, T. Hamann and J. Bisquert, Water oxidation at hematite photoelectrodes: The role of surface states, *J. Am. Chem. Soc.*, 2012, **134**, 4294-4302.
  19. Y. Zhang, H. Zhang, A. Liu, C. Chen, W. Song and J. Zhao, Rate-limiting O–O bond formation pathways for water oxidation on hematite photoanode, *J. Am. Chem. Soc.*, 2018, **140**, 3264-3269.
  20. Y. Zhang, H. Zhang, H. Ji, W. Ma, C. Chen and J. Zhao, Pivotal role and regulation of proton transfer in water oxidation on hematite photoanodes, *J. Am. Chem. Soc.*, 2016, **138**, 2705-2711.
  21. F. Ning, M. Shao, S. Xu, Y. Fu, R. Zhang, M. Wei, D. G. Evans and X. Duan, TiO<sub>2</sub>/graphene/NiFe-layered double hydroxide nanorod array photoanodes for efficient photoelectrochemical water splitting, *Energy Environ. Sci.*, 2016, **9**,

2633-2643.

22. S.-S. Yi, B.-R. Wulan, J.-M. Yan and Q. Jiang, Highly efficient photoelectrochemical water splitting: surface modification of cobalt-phosphate-loaded  $\text{Co}_3\text{O}_4/\text{Fe}_2\text{O}_3$  p-n heterojunction nanorod arrays, *Adv. Funct. Mater.*, 2019, **29**, 1801902.
23. P. S. Shinde, S. H. Choi, Y. Kim, J. Ryu and J. S. Jang, Onset potential behavior in  $\alpha\text{-Fe}_2\text{O}_3$  photoanodes: the influence of surface and diffusion Sn doping on the surface states, *Phys. Chem. Chem. Phys.*, 2016, **18**, 2495-2509.
24. A. G. Shard, Practical guides for x-ray photoelectron spectroscopy: quantitative XPS, *J. Vac. Sci. Technol. A*, 2020, **38**, 041201.
25. C. A. Mesa, L. Francàs, K. R. Yang, P. Garrido-Barros, E. Pastor, Y. Ma, A. Kafizas, T. E. Rosser, M. T. Mayer, E. Reisner, M. Grätzel, V. S. Batista and J. R. Durrant, Multihole water oxidation catalysis on haematite photoanodes revealed by operando spectroelectrochemistry and DFT, *Nat. Chem.*, 2020, **12**, 82-89.
26. Y. Zhao, C. Deng, D. Tang, L. Ding, Y. Zhang, H. Sheng, H. Ji, W. Song, W. Ma, C. Chen and J. Zhao,  $\alpha\text{-Fe}_2\text{O}_3$  as a versatile and efficient oxygen atom transfer catalyst in combination with  $\text{H}_2\text{O}$  as the oxygen source, *Nat. Catal.*, 2021, **4**, 684-691.
27. F. Le Formal, E. Pastor, S. D. Tilley, C. A. Mesa, S. R. Pendlebury, M. Grätzel and J. R. Durrant, Rate law analysis of water oxidation on a hematite surface, *J. Am. Chem. Soc.*, 2015, **137**, 6629-6637.

28. L. Wu, D. Tang, J. Xue, S. Wang, H. Ji, C. Chen, Y. Zhang and J. Zhao, Boosting multi-hole water oxidation catalysis on hematite photoanodes under low bias, *Sci. China Chem.*, 2023, **66**, 896-903.
29. M. Jadwiszczak, K. Jakubow-Piotrowska, P. Kedzierzawski, K. Bienkowski and J. Augustynski, Highly efficient sunlight-driven seawater splitting in a photoelectrochemical cell with chlorine evolved at nanostructured WO<sub>3</sub> photoanode and hydrogen stored as hydride within metallic cathode, *Adv. Energy Mater.*, 2020, **10**, 1903213.
30. P. J. Barczuk, A. Krolikowska, A. Lewera, K. Miecznikowski, R. Solarska and J. Augustynski, Structural and photoelectrochemical investigation of boron-modified nanostructured tungsten trioxide films, *Electrochim. Acta*, 2013, **104**, 282-288.
31. Y. Shi, Y. Li, X. Wei, J. Feng, H. Li and W. Zhou, Facile preparation of porous WO<sub>3</sub> film for photoelectrochemical splitting of Natural Seawater, *J. Electron. Mater.*, 2017, **46**, 6878-6883.
32. A. M. Rassoolkhani, W. Cheng, J. Lee, A. McKee, J. Koonce, J. Coffel, A. H. Ghanim, G. A. Aurand, C. Soo Kim, W. Ik Park, H. Jung and S. Mubeen, Nanostructured bismuth vanadate/tungsten oxide photoanode for chlorine production with hydrogen generation at the dark cathode, *Commun. Chem.*, 2019, **2**, 57.
33. S. Iguchi, Y. Miseki and K. Sayama, Efficient hypochlorous acid (HClO) production via photoelectrochemical solar energy conversion using a BiVO<sub>4</sub>-

- based photoanode, *Sustainable Energy Fuels*, 2018, **2**, 155-162.
34. S. Okunaka, Y. Miseki and K. Sayama, Improvement of photoelectrochemical HClO production under visible light irradiation by loading cobalt oxide onto a BiVO<sub>4</sub> photoanode, *Catal. Sci. Technol.*, 2021, **11**, 5467-5471.
35. W. Luo, Z. Yang, Z. Li, J. Zhang, J. Liu, Z. Zhao, Z. Wang, S. Yan, T. Yu and Z. Zou, Solar hydrogen generation from seawater with a modified BiVO<sub>4</sub> photoanode, *Energy Environ. Sci.*, 2011, **4**, 4046-4051.